Instabilities identification based on a new centrifugal 3D impeller outflow model

Meng Fan, Antoine Dazin, Gérard Bois, Francesco Romano

Instabilities identification based on a new centrifugal 3D impeller outflow model

Meng Fan *, Antoine Dazin, Gérard Bois, Francesco Romanò

Univ. Lille, CNRS, ONERA, Arts et Métiers Institute of Technology, Centrale Lille, UMR 9014-LMFL-Laboratoire de Mécanique des Fluides de Lille - Kampé de Fériet, Av. Paul Langevin, Villeneuve-d'Ascq, Lille, F-59000, Hauts de France, France

A B S T R A C T

Previous research works have shown that the inflow boundary conditions have a significant effect on the behavior of diffusers in a centrifugal machine. To better understand the vaneless diffuser instability mechanism and save computing resources, several numerical works are planned to be conducted for the solely vaneless diffuser, excluding the rest of the centrifugal machine from the flow domain to simulate. Previous reduced-order models used either two-dimensional approaches that focused exclusively on the core-flow instability or three-dimensional models tested for a few inflow conditions. To obtain the more realistic diffuser inlet boundary conditions, a modeling method is here developed by fitting the diffuser inflow velocity derived from numerical simulations of the entire machine. The classic fitting methods used to approximate inflow profiles by algebraic polynomials or Gaussian functions are observed to introduce numerical artifacts that significantly affect the flow and therefore its stability. The multi-stage scale-matching fitting approach developed in this study is designed as a robust successive-order approximation of the inflow conditions. Our objective is to demonstrate its robust capability of taking into account the main physical features of the inlet velocity profiles, which, in turn, allows us to significantly improve the prediction of the flow instability occurring in the pump diffuser. Firstly, the RANS and URANS simulations of the entire machine are carried out by OpenFOAM using the $k-\omega$ SST turbulence model. The simulation results show that the RANS simulation is efficient in correctly capturing the diffuser inlet velocity profile except for developed stall conditions. The RANS simulations are carried out for cases with three different kinds of leakage configurations between the impeller and the diffuser. For each case, five flow rates were simulated to get the basic data for fitting the inlet profiles for a total of 125 simulations. The diffuser inlet velocity profiles are averaged in the azimuthal direction and fitted such to obtain an explicit function for the azimuthally-averaged velocity profile that varies with the flow rate Q. The fitting results are very close to the original data, and using our fits to predict the diffuser flow instabilities we show that our modeling approach compares well against the URANS simulations of the whole machine.

1. Introduction

The vaneless diffuser of any radial, mixed flow compressor or pumps acts to properly reduce the mean flow velocity and gain static pressure along its path. As for two-dimensional parallel wall diffusers, too rapid a diffusion process leads to important flow separations, whereas too low a diffusion rate increases the friction losses due to excessive flow path length of the mean flow. Large or uncontrolled diffusion limits diffuser performances and induces stall with specific unsteady phenomena that have been explained and described by several authors like Jansen [1] and Japikse [2].

For a constant vaneless diffuser width, the mean streamline path length is directly related to the evolution of the absolute flow angle α between the mean absolute velocity and the tangential direction. The diffuser inlet flow angle value depends on initial asymmetric velocity components delivered by the impeller, the values of which depend on the compressor Reynolds number, March number, impeller design, and more specifically specific speed. The prediction of the diffuser "inlet critical mean flow an-

* Corresponding author.
E-mail address: meng.fan@ensam.eu (M. Fan).

gle" for which stall may occur is the main parameter research target that has been investigated in past decades. The vaneless diffuser stall mechanism has indeed been studied by many researchers. Most analytical models are based on two different approaches:

1. Boundary layer momentum integral equation to relate rotating stall with radial reverse flow inside the boundary layer (see Jansen [1], Senoo & Kinoshita [3], and Frigne & Van den Braembussche [4]),
2. Inviscid core flow instability analysis (see Tsujimoto et al. [5], Abdelhamid [6], Moore [7], and Ljevar et al. [8]).

Both situations can be found in radial fans, centrifugal pumps, industrial compressors, and aerospace applications for air-breathing engines, airplane conditioning units, or cryogenic rocket multi-stage pumps, depending on design-specific speeds. Diffusers with a large aspect ratio (defined as $\chi = b_3/(R_4 - R_3)$, where R_3 denote the diffuser inlet radius, R_4 denote the diffuser outlet radius, and b_3 denotes the diffuser constant width) and a small aspect ratio respond differently to variations of a given parameter. Most of the relevant experimental and numerical contributions can be found in the review section performed by Gao et al. [9]. They performed a statistical analysis of the geometrical effects on the rotating stall. They confirm that the critical flow angle value mainly depends on the diffuser geometry and more specifically the diffuser aspect ratio and the radius ratio (defined as $\Gamma = R_4/R_3$). The stall cell number and location also depend on diffuser geometry and flow parameters. In their conclusion, Gao et al. [9] suggest the possible existence of two mechanisms that could be responsible for the occurrence of instability in the impeller and diffuser combinations. Dou & Mizuki [10] and Abdelhamid [6] try to combine the above two approaches and concluded that stall mechanisms were different for the narrow diffusers and wide diffusers. However, no one can clearly define the frontier between narrow and wide diffusers.

This reinforces the idea of paying attention to more detailed inlet boundary conditions at the impeller outlet plane including non-uniform flow. In this respect, an interesting sensitivity analysis has been recently presented by Hu et al. [11] using four typical asymmetric inlet radial flow conditions associated with a constant tangential velocity component in the core region as the initial condition for the diffuser. This study was conducted for three different diffuser aspect ratios below 0.14 (which is despite everything being considered as a relatively small value) but only for one flow coefficient corresponding to a core flow angle close to 20 degrees.

The present paper deals with a higher diffuser constant aspect ratio of about 0.3 combined with a radius ratio of about 1.50. The complete 3D velocity profile at the impeller outlet section is taken as initial conditions at the diffuser inlet section using a fitting technique described in detail. It better describes the real radial and tangential asymmetric inflow conditions compared with the simplified one adopted by Hu et al. [11]. The radius ratio has been enlarged compared with the optimal value to favor the instabilities development. Several experimental investigations on the whole model including a shrouded impeller and diffuser have been already presented in several papers listed in the next section. This study aims to develop and validate a low-computationally-intensive approach that relies on a reduced-order diffuser inflow model. Compared with a fully 3D URANS one, our method could better suit future diffuser designs and fundamental studies with respect to unsteady modes occurring in vaneless diffusers.

Fitting techniques are widely used to provide boundary conditions for reduced-order model simulations. Emvin et al. [12] developed a simple approach for a diffuser simulation using a momentum method for approximation of the inlet velocity. All the inlet jets are replaced by the momentum and mass boundary conditions over the diffuser plate. Such a momentum method is suitable for coarse meshes and cannot accurately reproduce some of the mean inflow features of the diffuser inlet profile such as the boundary layers for the mean flow and the swirl. Deng et al. [13] performed the momentum equation discretization for the first cell adjacent to the diffuser. Their velocity algebraic equation is expressed as a diffuser-related term and a diffuser-nonrelated term. Based on the analysis of the diffuser-related term, a total-flux momentum method helps minimize the computational error and reduces the effort required to determine an optimal grid. Other reduced-order models used either two-dimensional approaches that focused exclusively on the core-flow instability [5,8] or three-dimensional models tested for a few inflow conditions [11]. The multi-stage fitting approach we propose in this study is intended to provide inflow conditions for the diffuser regardless of the local computational grid. To do so, we develop a multi-stage fitting method that focuses on one specific scale per fitting stage and then matches them in a final fitting step that returns the fitted velocity profile in analytical explicit form. This approach allows us to introduce the theoretical local scaling at the boundary layers, which inherently separates the boundary layer scale from the bulk flow. This could be of help for future analyses that will attempt to use asymptotic matching and can compare the theoretical prediction with our fitting coefficients. None of the previous techniques adopted a scale-matching-like approach for their fitting. This is the original contribution of our fitting technique and it does not suffer from spurious oscillations typical of classic fitting methods. Having a multi-stage fitting approach allows for building a model capable of identifying successive approximations of the inflow condition. Once again, this follows the typical logic used in asymptotic theory and helps identify and interpret the effects that determine the velocity inlet profile.

This paper is structured as follows: Section 2 defines the mathematical model, assuming low Mach number conditions (incompressible flow), Sec. 3 presents the discretization employed to numerically solve the Navier–Stokes system, Sec. 4 explains the method to approximate the azimuthally averaged vaneless diffuser inlet velocity profiles as explicit functions of the flow rate Q. The results including the fitted velocity profiles and the numerical simulations based on the fitted profiles as inlet boundary conditions are presented and tested in Sec. 5. Finally, in Sec. 6 the results are summarized, discussed, and conclusions are drawn.

2. Methodology

2.1. Geometry model

The study investigates the effect of leakage flow between the impeller and diffuser on incompressible airflow in a radial flow machine. The entire computational domain which includes the inlet pipe (yellow), the centrifugal impeller (gray), the vaneless diffuser (dark green), and a radial outflow box (light green) is depicted in Fig. 1. The outflow box is placed at the outlet of the diffuser to prevent the outflow boundary conditions from being applied too close to the centrifugal machine. The numerical model used in the study reproduces the geometry and flow conditions of our experimental set-up described in detail in Appendix B. The main parameters of the radial impeller

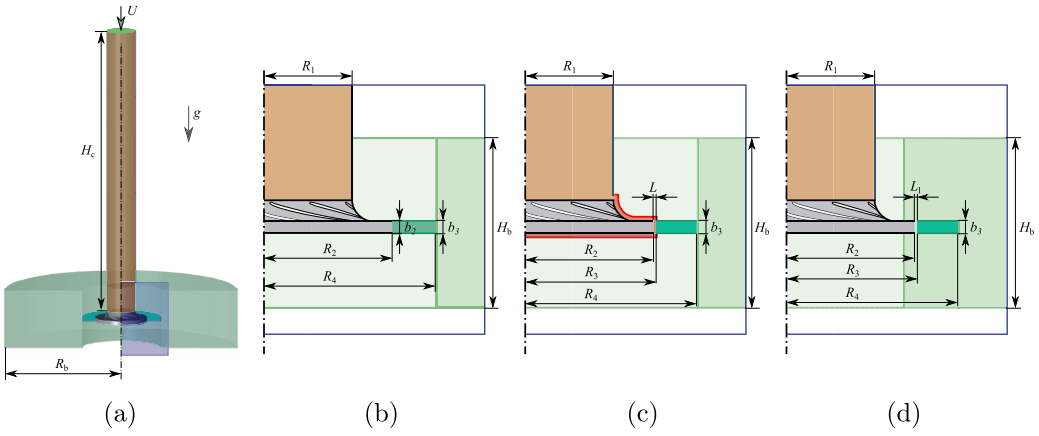

Fig. 1. Schematic of (a) the entire computational domain for the radial flow machine and the zoom-in view of the three computational configurations: (b) zero-, (c) negative-, and (d) positive-leakage case. (For interpretation of the colors in the figure(s), the reader is referred to the web version of this article.)

Table 1
Main geometrical characteristics of the impeller and diffuser model. The CAD of the impeller is uploaded on https://github.com/fromano88/CentrifugalPump.git.

Impeller characteristics		
R_1	Tip inlet radius (shroud side)	141.1 mm
R_{1h}	Tip inlet radius (hub side)	96.9 mm
R_2	Outlet radius	257.5 mm
b_2	Outlet width	38.5 mm
Z	Number of blades	7
β_{2c}	Outlet blade angle	22.5°
K	Mean blade thickness	9 mm
R_{c1}	Casing inlet radius (negative-leakage case)	143.675 mm
R_{c2}	Casing outlet radius (negative-leakage case)	260.075 mm
Q_d	Design flowrate (1200 rpm)	0.236 m^3/s
$Re = R_2{}^2\omega_{imp}/\nu$	Reynolds number	5.52×10^5
$Ma = R_2\omega_{imp}/c$	Mach number (Q/Q_d = 1.0, ω = 125 rad/s)	0.095
Diffuser characteristics		
R_3	Inlet radius (zero-leakage case)	257.5 mm
	Inlet radius (negative-leakage case)	260.075 mm
	Inlet radius (positive-leakage case)	260.075 mm
R_4	Outlet radius	385.5 mm
b_3	Constant width	38.5 mm
Γ	Radius ratio	≈1.50
χ	Aspect ratio	≈0.3
α_m	Inlet mean flow angle (Q/Q_d = 1.0)	≈14°

and vaneless diffuser are provided in Table 1. Three different leakage configurations are simulated in the study, referred to as zero-, negative-, and positive-leakage cases, depending on the direction of the leakage flow entering the diffuser:

Zero-leakage: corresponds to a simplified configuration. The radial gap between the impeller and the vaneless diffuser is set to zero, which means there is no leakage between the two components (see Fig. 1(b)). Also, there are no axial gaps between the inlet-pipe outlet and the impeller inlet, ensuring no leakage in this area;

Negative-leakage: corresponds to a usual centrifugal machine configuration, there is a small gap between the impeller and the vaneless diffuser, which allows for leakage flow from the outlet to inlet sections of the impeller. Consequently, a radial gap $L = R_3 - R_2$ is introduced in Fig. 1(c); Furthermore, a casing of height L is added to prevent leakage flows.

Positive-leakage: qualitatively reproduced the experimental geometry in the corresponding numerical simulations (see Fig. 1(d)). The axial gap between the outlet of the inlet pipe and the inlet of the impeller is not taken into consideration. All the comparisons between experiments and numerical performance are considered for the positive-leakage case, employed for validation of our numerics.

The inlet boundary condition is defined at the entrance of the circular pipe that connects to the impeller. The height of the pipe H is 10 times the impeller tip inlet radius R_1. A radial outflow box (dark pink) is introduced at the outlet of the diffuser to prevent the outflow boundary conditions from being applied too close to the machine. The height of this box H_b is 15 times its width b_3 and its radius R_4 is three times the radius of the diffuser outlet R_3.

2.2. Problem fomulations

In the computational domain of our problem, the mass, momentum and energy conservation equations are solved in the form of steady (RANS) and unsteady Reynolds-averaged Navier–Stokes (URANS) equations. The URANS equations are

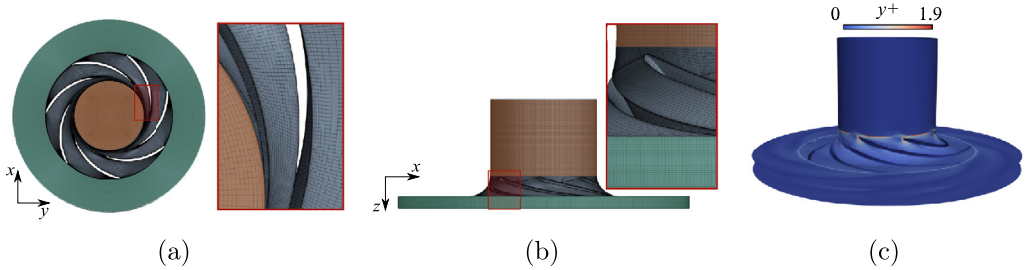

Fig. 2. Top view (a) and side view (b) of a typical mesh of the zero-leakage case used to perform the three-dimensional numerical simulations, and (c) an example of the y^+ distribution on the walls.

$$\frac{\partial \vec{U}}{\partial t} + (\vec{U} \cdot \nabla)\vec{U} + \nabla P = \nabla \cdot (2\nu \vec{\vec{S}} - \vec{\vec{\tau}}), \quad \nabla \cdot \vec{U} = 0, \tag{1}$$

where $\vec{U} = \vec{U}(\vec{x};\ t) = (U_1, U_2, U_3)$ denotes the mean part of the velocity vector, $P(\vec{x}; t)$ is the mean pressure divided by the fluid density, ν is the constant kinematic viscosity, $\vec{x}$ is the position vector, t denotes the time, $\vec{\vec{S}} = \frac{1}{2}(\nabla \vec{U} + \nabla^T \vec{U})$ is the mean rate of the strain tensor, and $\vec{\vec{\tau}}$ is the Reynolds stress tensor. The values of the Reynolds stress in the (U)RANS equations are computed by the SST $k-\omega$ turbulence model which is commonly employed for dealing with turbomachines. This model has shown the capability to capture the key flow features at the core of our study [14,15]. Detailed information about the turbulence model is given by Menter [16].

3. Computational setup

3.1. Mesh generation

Hexahedral cells are a popular choice for meshing in computational fluid dynamics (CFD) simulations because they are less costly and less diffusive compared with tetrahedral cells, particularly near the boundary layers. ANSYS ICEM-CFD is a commercial software that is utilized for creating meshes. The multi-block structure used in ICEM-CFD allows for flexibility and accuracy in the mesh generation process. A mesh with 2.3 million finite volumes was chosen for RANS and URANS simulations of the whole machine after conducting a grid-independent verification using four grids (details in Appendix C). Meanwhile, to ensure the accuracy of the boundary layer calculation, three different boundary layer meshes are tested (details in Appendix C). The mesh we chose in the near-wall regions is refined with an expansion ratio of 1.5 as shown in Fig. 2(a–b) to keep the y^+ values close to 1 on the walls in the inlet pipe, impeller, and vaneless diffuser domains (see Fig. 2(c)). The sole areas where the y^+ is of order 1 (still lower than 2) are at the leading edges of the impeller blades, where the flow curvature is too high to attempt a localized refinement without incurring excessive grid stretching. We further stress that in the areas of interest, hence all over the diffuser walls and the rest of the impeller blades, our y^+ is below 1.

The mesh is then converted to a format readable by OpenFOAM using the converter, `fluent3DmesToFoam`. The same mesh excluding the impeller and inlet pipe regions are used for the simulation of the sole diffuser in our latter work. Besides, to better carry out the fitting work of the velocity profiles presented in the following sections, additional RANS simulations with the 5.4M cells mesh were carried out to assure a sufficient amount of cells along the diffuser height direction.

3.2. Numerical method

In this work, the Mach number $Ma = R_2\omega_{\text{imp}}/c$ = 0.095 $\ll$ 0.3, where ω_{imp} is the rotation rate of the impeller and c = 340 m/s the speed of sound. More details on the local distribution of the Mach number across the starting phase from rest and under fully-developed conditions are given in Appendix A. The incompressible Navier-Stokes equations were solved using the $k-\omega$ SST turbulence model in OpenFOAM v1912 based on a turbulence model independence analysis (details in Appendix D). The high-order advection scheme and second-order backward Euler transient scheme were employed. The selected solvers are `pimpleFoam` and `simpleFoam` for transient and steady incompressible flows, respectively. The discretization is based on a finite volume approach, where both the convective and the diffusive terms are approximated by second-order centered schemes. A second-order Crank-Nicolson method [17] is used for time integration. The transient solver makes use of the solution algorithm PIMPLE, a cross-over merging the PISO and SIMPLE algorithms. For steady simulations, we use the algorithm SIMPLE. A generalized geometric-algebraic multi-grid (GAMG) method with a tolerance of 10^{-7} is used to solve the linear system for the pressure equations. Boundary conditions are implemented using the standard OpenFOAM capabilities, while the outflow boundaries use the `inletOutlet` boundary type.

The inlet velocity corresponding to a pre-set value of inlet flow rate Q is specified using a Dirichlet type boundary condition named `flowRateInletVelocity`, and the static pressure p = 0 Pa is set for the outlet at the outflow contours far away from the diffuser outlet. The `noslip` wall boundary is applied to fixed walls, and the `rotatingWallVelocity` boundary condition which specifies a rotational velocity is used for rotating walls.

The initial boundary conditions used for URANS simulation were taken from the RANS simulation results in order to disregard the flow's startup phase in the simulation. The rotational speed was set as 125 rad/s and the time step Δt, corresponds to 0.5° of the impeller revolution. The simulation results give a mean Courant number for the whole domain of $\overline{C} = 0.0075$ at the design condition. RANS simulations were run for ten thousand time steps to ensure convergence of the SIMPLE algorithm. URANS simulations were run for 70 revolutions of the impeller, and all URANS results presented in the paper are either from the last time step or a phase average of the last impeller revolution. For more details of the numerical settings, refer to Fan et al. [14].

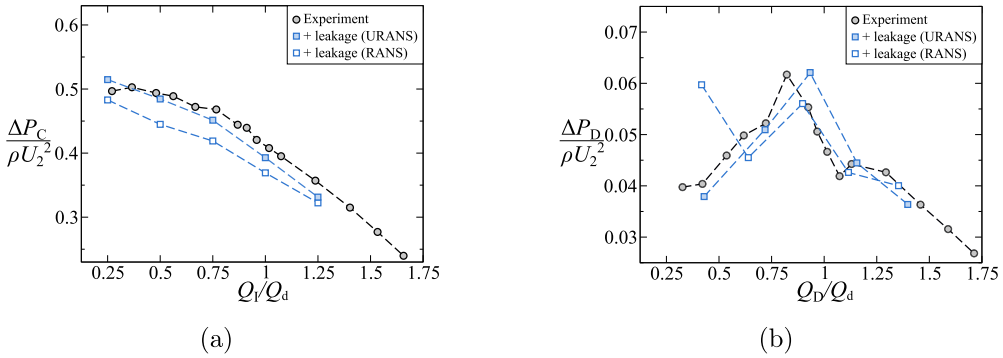

Fig. 3. Performance curves of (a) entire machine and (b) diffuser for the positive-leakage case obtained from experimental and numerical simulation results.

3.3. Validation of the numerical method

As an extended study that originated in the LMFL laboratory. A detailed experimental database is available to the authors thanks to our previous studies [15] and is here used for the validation of numerical results. The numerical results of the positive-leakage case using 2.3M cells mesh are firstly validated against the experimental results since this geometrical configuration of our simulations is the closest to the experimental set-up. The performance of the entire machine, encompassing the impeller and the diffuser, as well as the performance of the sole diffuser evaluated in terms of static pressure rise obtained from the RANS and URANS simulations are compared with the experimental results respectively in Fig. 3(a,b). Note that Q_I and Q_D denote the volume flow rate of the impeller and the one of the vaneless diffuser respectively, which takes the leakage flow effect into account (see Fan [15]). As expected, the entire machine performance obtained from the URANS simulation better agrees with the experimental results (see Fig. 3(a)), as they capture the slowest time scales of the flow dynamics. Concerning the diffuser performance (see Fig. 3(b)), the results of both the RANS and the URANS simulations are acceptable at large flow rates. But at the smallest flow rate, the RANS simulation results are very different from the URANS and experimental results. This is result from the rotating stall phenomena occurring in the vaneless diffuser which can not be captured by the steady-state calculations (for more details, we refer to Fan et al. [14]).

Fig. 4 shows the comparison of the radial, tangential, and axial velocity profile with the impeller rotational speed $\omega_{\text{imp}} = 125$ rad/s and the diffuser radius ratio $\Gamma = 1.50$ obtained by RANS with 2.3M cells and 5.4M cells and URANS with 2.3M cells at the flow rate $Q/Q_d = 1.25,\ 1.00,\ 0.75,\ 0.50,$ and 0.25. Note that in all the color maps of this study, the velocities U_*, static pressures P, and z coordinates are nondimensionalized by

$$\hat{U}_* = \frac{U_*}{U_2}, \qquad \hat{P} = \frac{P}{\frac{1}{2}\rho {U_2}^2}, \qquad \hat{z} = \frac{z}{b_3} \tag{2}$$

where $* \in \{r, \theta, z\}$, $U_2 = \omega_{\text{imp}} R_2$ is a characteristic velocity in this problem, and b_3 is the constant diffuser width. It can be observed that at the large flow rate, the profiles obtained from the RANS simulation are very close to the URANS ones. With the decrease in the flow rate, the deviation between the RANS and URANS increases. This is because the RANS simulation can not capture the rotating instability that occurs in the vaneless diffuser at such low flow rates, hence it further confirms our interpretation of the deviation of the entire machine performance predicted by RANS simulations. Fig. 4 also demonstrates that the profiles obtained by the RANS simulation with 2.3M and 5M cells show good convergence.

4. Fitting the boundary condition at the diffuser inlet

In order to model the diffuser inflow, a parametric fitting protocol will be employed, based on three underlying assumptions:

- The fitting protocol assumes that the inlet flow conditions of the vaneless diffuser can be extracted from solely tangentially averaged RANS simulation results for several flow rates.
- It is implicitly assumed that no mutual interactions are present between an impeller and the vaneless diffuser as far as rotating instabilities are concerned. This is further motivated by the study of flow instabilities [14], whose mechanism is related to the flow behavior solely inside the diffuser itself.
- The three velocity components at the impeller outlet will be fitted with explicit analytical functions.

The validation of the numerical results to fit has been recently published by Fan et al. [14] and is based on the comparisons between fully 3D URANS simulations and experimental results. In Fan et al. [14], a detailed analysis of the effect of inlet boundary conditions on the instability patterns, including leakages between the impeller-diffuser gap, has been carried out. Building on the fitting developed in this study, we will be capable of further controlling the diffuser inflow and perturb it ad hoc to study the effect of first harmonic modulations on the mean inflow obtained via the fit.

4.1. Model simplification

A simplified simulation approach is proposed here to allow for a parametric investigation of the flow in the vaneless diffuser at an affordable computational cost. Fig. 5(a) depicts the three-dimensional computational domain of the simplified model: the inlet pipe

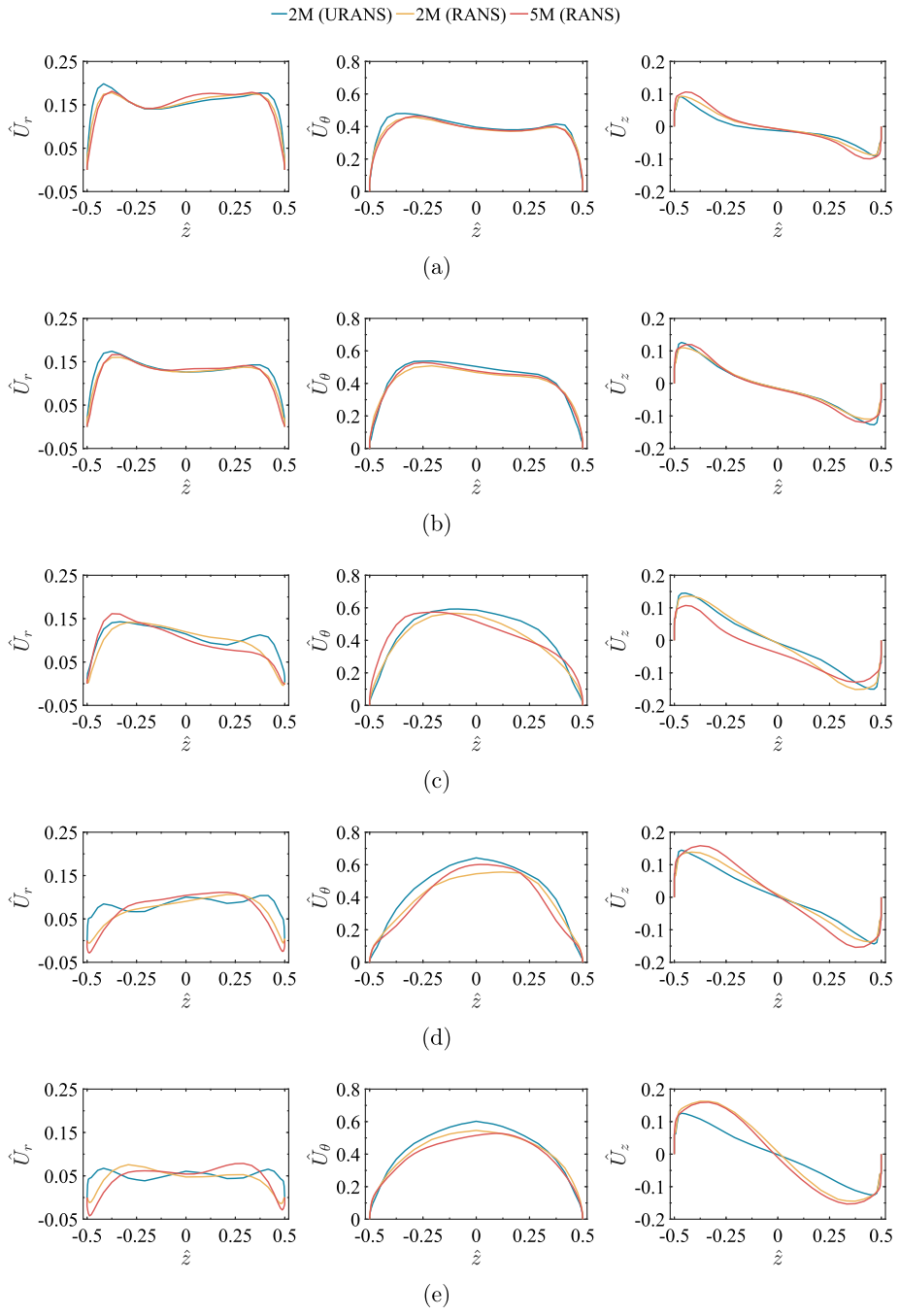

Fig. 4. Comparison of the diffuser inlet radial, tangential, and axial velocity profile with the rotational speed $\omega_{\text{imp}} = 125$ rad/s and the diffuser radius ratio $\Gamma = 1.50$ obtained from RANS with 2 million mesh and 5 million mesh and URANS at five different flow rates: (a) $Q/Q_d = 1.25$, (b) $Q/Q_d = 1.00$, (c) $Q/Q_d = 0.75$, (d) $Q/Q_d = 0.50$, and (e) $Q/Q_d = 0.25$.

and the rotating impeller have been removed, and only the vaneless diffuser and the outflow box are simulated. To reproduce the inlet boundary conditions, the diffuser inlet velocity profile is fitted as a function of the flow rate $\hat{Q} = Q/Q_d$, using the RANS simulation results as a fitting database. We start by fitting the flow profiles azimuthally averaged at the diffuser inlet. To fit the z-dependent inlet velocity profile $\vec{U}(z)$, the full range $z \in [-h/2, h/2]$ is subdivided into two boundary layer regions and a bulk flow region (see Fig. 5(b)). The two boundary regions are fitted with a power-law function, and their thickness δ_i is numerically determined by finding the length that allows fitting the boundary layer at best. The velocity component $U_*(z)$, where $*$ denotes the r, θ, and z direction, is approximated by dedicated functional dependencies within each region according to

$$\text{Boundary region 1,} \qquad z \in [z_{\min}, z_{\min} + \delta_1]: \quad U_* \approx a_{*0} \left(\frac{h}{2} + z \right)^{a_{*1}}, \tag{3a}$$

$$\text{Boundary region 2,} \qquad z \in [z_{\max} - \delta_2, z_{\max}]: \quad U_* \approx b_{*0} \left(\frac{h}{2} - z \right)^{b_{*1}}, \tag{3b}$$

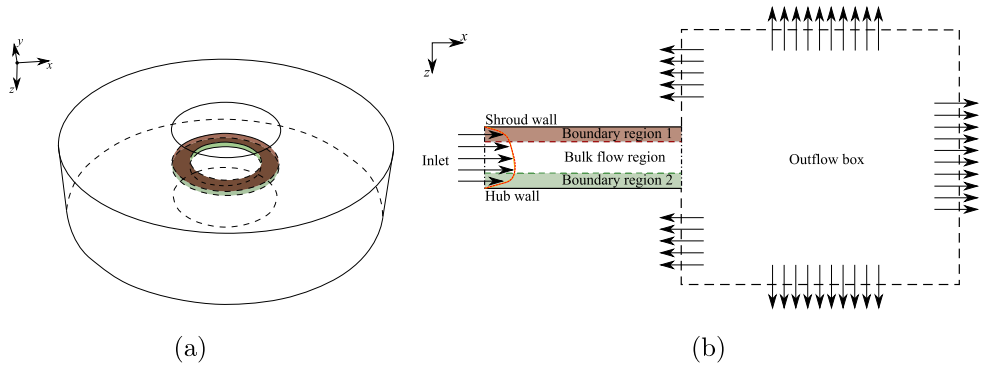

Fig. 5. Schematic of (a) the entire computational domain for the model flow (diffuser shroud and hub walls are marked in red and green respectively) and (b) the meridian section of the simplified numerical model. Note that the outflow box in (b) is not drawn in scale.

$$\text{Bulk flow region,} \qquad z \in [z_{\min} + \delta_1, z_{\max} - \delta_2]: \quad U_* \approx U_*^{\text{bulk}}(z), \tag{3c}$$

where the thickness of the boundary layer regions δ_i is specified for different cases, h denotes the width of the diffuser, a_{*0} and b_{*0} are fitting coefficients, $U_*^{\text{bulk}}(z) = \sum_{i=1}^{n} U_*^{\text{bulk,i}}(z)$ consists of the sum of a linear, a quadratic, a fourth power, and/or a trigonometric function as detailed below.

4.2. Fitting protocol

The fitting has been carried out for five diffuser radius ratios Γ and five rotational speeds ω_{imp} with our three different leakage configurations. For each case, the functional dependence of the coefficients of (3) is derived following a multi-stage algorithm. All coefficients required for the approximation of $U_*(z)$ are determined by minimizing the squared distances between the data and the fit functions within their respective regions. Since the fit functions are nonlinear, a Newton method is employed to solve the non-linear equations governing the least-squares minimization operation. This procedure requires providing an initial guess sufficiently close to the solution and defining a termination criterion for the iteration. The iteration is considered converged when the residual of the fit coefficients is less than 10^{-8} in the absolute norm.

As an example, the fitting steps of the diffuser inlet radial velocity $U_r(z)$ (positive-leakage case) are explained below. Each fitting step consists of multiple stages, and the algorithms are explained in the form of flow charts in Figs. 6 to 11.

Step I: fits the two boundary layer regions with the power law function (eqs. (3a) and (3b)), the final form reads:

$$U_r^{\text{bl1}}(z) = \underbrace{a_{r0}\left(\frac{h}{2} + z\right)^{a_{r1}}}_{\text{boundary region 1}} \left\{ \frac{\tanh\left[a_{r2}\left(c_{\text{rbl1}} - \frac{h}{2} - z\right)\right] + 1}{2} \right\}, \tag{4}$$

$$U_r^{\text{bl2}}(z) = \underbrace{b_{r0}\left(\frac{h}{2} - z\right)^{b_{r1}}}_{\text{boundary region 2}} \left\{ \frac{\tanh\left[b_{r2}\left(c_{\text{rbl2}} - \frac{h}{2} - z\right)\right] + 1}{2} \right\}, \tag{5}$$

where $c_{\text{rbl}i}$ are coefficients specified to control the thickness of the two boundary layers δ_i. As explained in the flow chart in Fig. 6, the algorithm consists of four stages:

Stage 1. The six coefficients $\dagger_{ri}$ (where $\dagger \in \{a, b\}$, $i \in \{0, 1, 2\}$) in the first fit functions are determined by fitting the numerical data $U_r^{\text{num}}(z)$ for each triple $(\Gamma, \omega_{\text{imp}}, \hat{Q})$ with $\Gamma \in \{1.25, 1.50, 1.75, 2.00, 2.50\}$, $\omega_{\text{imp}} \in \{10, 40, 75, 125, 180\}$ rad/s and $\hat{Q} \in \{0.25, 0.50, 0.75, 1.00, 1.25\}$.

Stage 2. Two of the six coefficients $\dagger_{r2}$ obtained in Stage 1 are updated by a secondary fit such that they depend on the flow rate $\hat{Q}$ (see Fig. 12(c)). This yields the corresponding coefficients $A^j_{\dagger_{r2}}$ $(j = 0, 1, 2)$ for $\dagger_{r2}$. The remaining four coefficients, obtained in Stage 1 are corrected by again fitting the numerical velocity function $U_r^{\text{num}}(z)$ in each respective region and for each combination of $\Gamma \in \{1.25, 1.50, 1.75, 2.00, 2.50\}$, and $\omega_{\text{imp}} \in \{10, 40, 75, 125, 180\}$ rad/s and $\hat{Q} \in \{0.25, 0.50, 0.75, 1.00, 1.25\}$ using the same function of Stage 1, but replacing the coefficients $\dagger_{r2}$ with the fitted values $\tilde{\dagger}_{r2}$.

Stage 3. The third iteration of two of the remaining four coefficients $\dagger_{r0}$ in each fit is obtained by fitting the second iteration for the coefficients $\dagger_{r0}$ in $\hat{Q}$ (see Fig. 12(b)). This yields the corresponding coefficients $A^j_{\dagger_{r0}}$ $(j = 0, 1, 2)$ for $\dagger_{r0}$. The remaining coefficients $\dagger_{r1}$ are then determined a third time by fitting to the numerical velocity function $U_r^{\text{num}}(z)$ for each combination of $\Gamma \in \{1.25, 1.50, 1.75, 2.00, 2.50\}$ and $\omega_{\text{imp}} \in \{10, 40, 75, 125, 180\}$ rad/s and $\hat{Q} \in \{0.25, 0.50, 0.75, 1.00, 1.25\}$ using the same function of Stage 1, but replacing $\dagger_{ri}$ with $\tilde{\dagger}_{ri}$ for $i = 0, 2$.

Stage 4. Finally, the coefficients $\dagger_{r1}$ are updated by fitting in flow rate $\hat{Q}$ (see Fig. 12(c)). This yields the coefficients $A^j_{\dagger_{r1}}$ $(j = 0, 1, 2, 3, 4)$ for $\dagger_{r1}$.

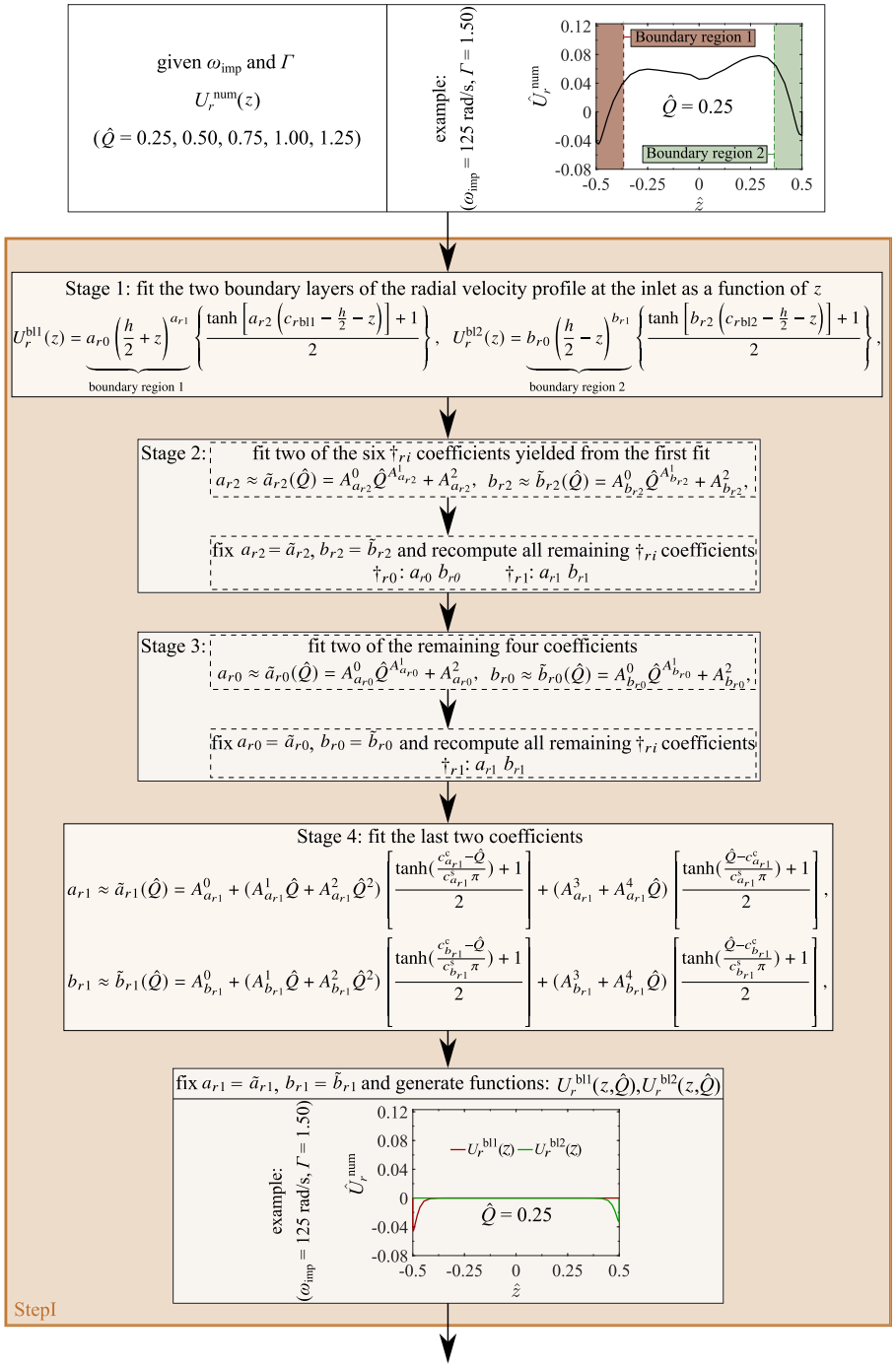

Fig. 6. Flowchart of the first fitting step for the radial velocity function. In output of this step we determine U_r^{bl1} and U_r^{bl2} as explicit functions.

By this procedure, a first set of coefficients $\dagger_{ri}$ (where $\dagger \in \{a, b\}, i \in \{0, 1, 2\}$) is obtained in Stage 1. The dependence on $\hat{Q}$ is then subsequently introduced in Stages 2, 3, and 4 for $\dagger_{r2}$, $\dagger_{r0}$, and $\dagger_{r1}$, respectively. With all the coefficients $A^j_{\dagger_{ri}}$ yielded from secondary fitting, the functions $U_r^{bl1}(z, \hat{Q})$ and $U_r^{bl2}(z, \hat{Q})$ can be generated.

Step II: fits the bulk flow part remaining from Step I

$$U_r^{dif1}(z) = U_r^{num}(z) - U_r^{bl1}(z) - U_r^{bl2}(z), \tag{6}$$

using a fourth power function combined with a trigonometric function

$$U_r^{bulk1}(z) = \underbrace{c_{r0}\left[z^4 - \left(\frac{h}{2}\right)^4\right]}_{\text{full range}} + \underbrace{c_{r1}\cos\left(\frac{2\pi}{h}z + \frac{\pi}{2}\right)}_{\text{bulk flow region}} \left\{\frac{\tanh\left\{c_{r2}\left[\frac{h}{2} - 20\left(\frac{c_{rbl1}+c_{rbl2}}{2}\right)^2 - z^2\right]+1\right\}+1}{2}\right\}, \tag{7}$$

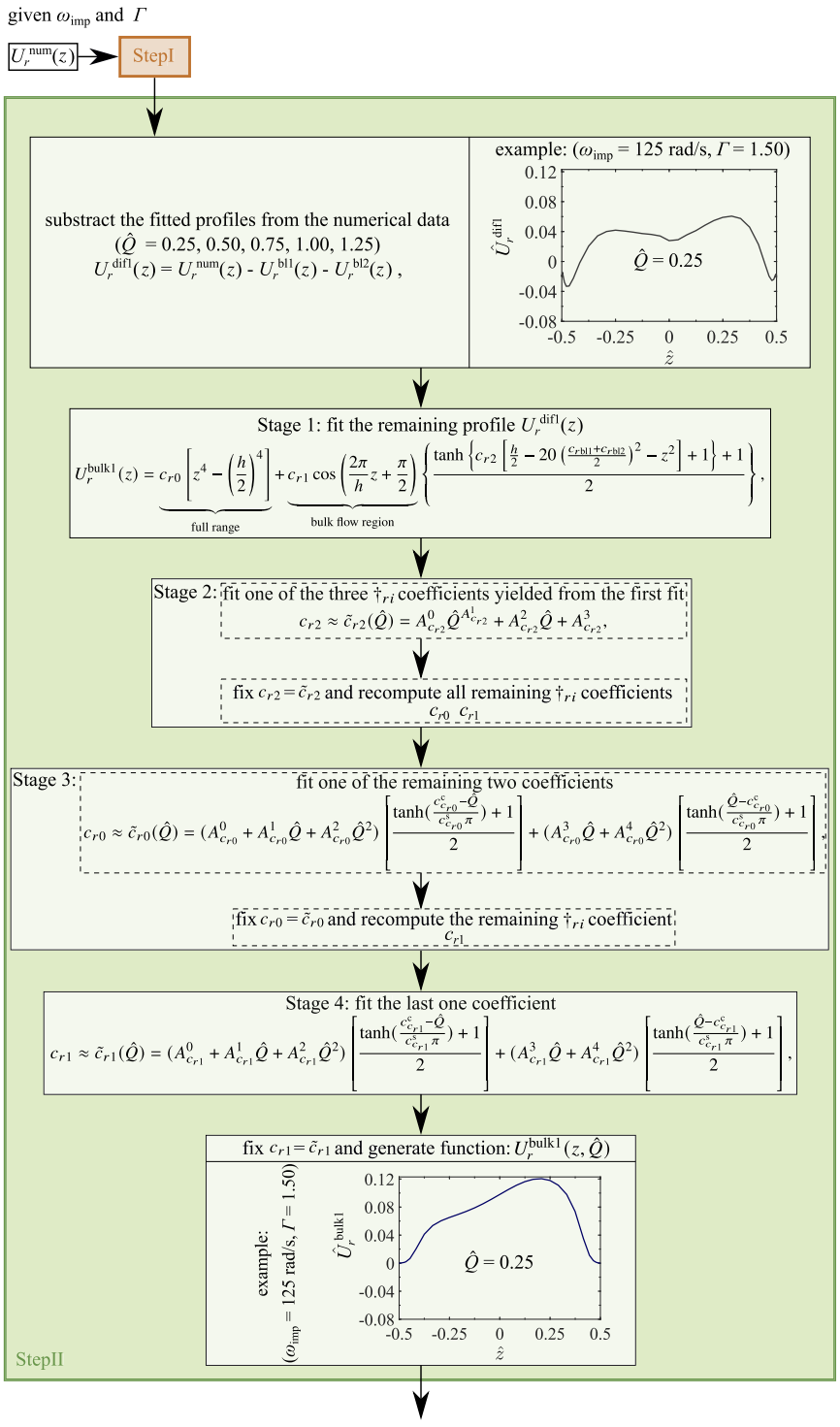

Fig. 7. Flowchart of the second fitting step for the radial velocity function. In output of this step we determine U_r^{bulk1} as an explicit function.

the fitting procedure of this step follows formally the same stages as in Step I (see Fig. 7).

Step III: fits the bulk flow part remaining from Step I and Step II

$$U_r^{dif2}(z) = U_r^{num}(z) - U_r^{bl1}(z) - U_r^{bl2}(z) - U_r^{bulk1}(z), \tag{8}$$

using a quadratic function combined with a trigonometric function

$$U_r^{bulk2}(z) = \underbrace{d_{r0}\left[z^2 - (\frac{h}{2})^2\right]}_{\text{full range}} + \underbrace{d_{r1}\cos\left(\frac{2\pi}{h}z + \frac{\pi}{2}\right)}_{\text{bulk flow region}}\left\{\frac{\tanh\left\{d_{r2}\left[\frac{h}{2} - 50\left(\frac{c_{rbl1}+c_{rbl2}}{2}\right)^2 - z^2\right] + 1\right\} + 1}{2}\right\}, \tag{9}$$

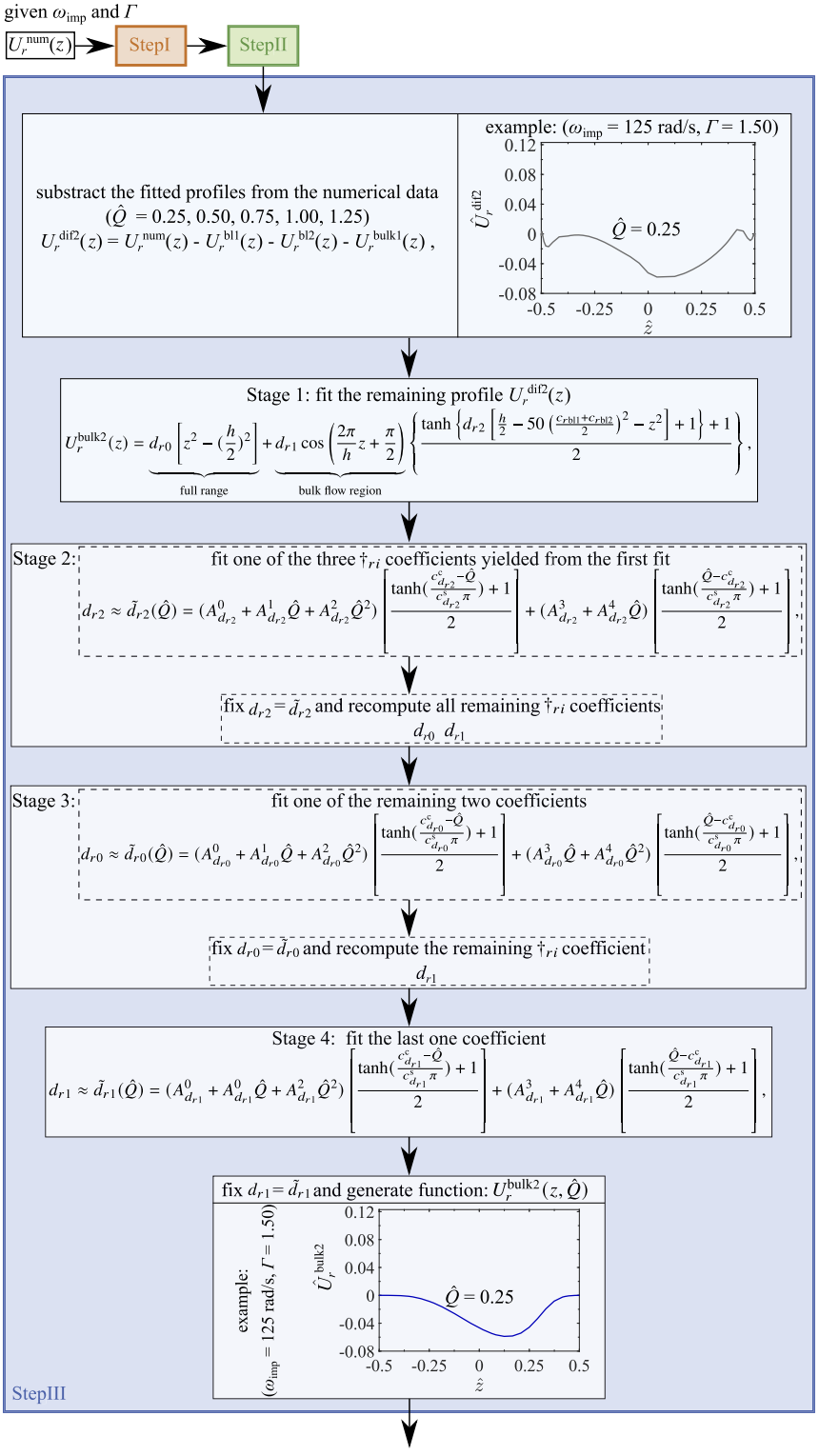

Fig. 8. Flowchart of the third fitting step for the radial velocity function. In output of this step we determine U_r^{bulk2} as an explicit function.

the fitting procedure of this step follows formally the same stages as in Step I and Step II (see Fig. 8).

Step IV: corrects for the high-order approximation at the boundaries by fitting the profile remaining from the previous three steps

$$U_r^{dif3}(z) = U_r^{num}(z) - U_r^{bl1}(z) - U_r^{bl2}(z) - U_r^{bulk1}(z) - U_r^{bulk2}(z), \tag{10}$$

using Gaussian functions

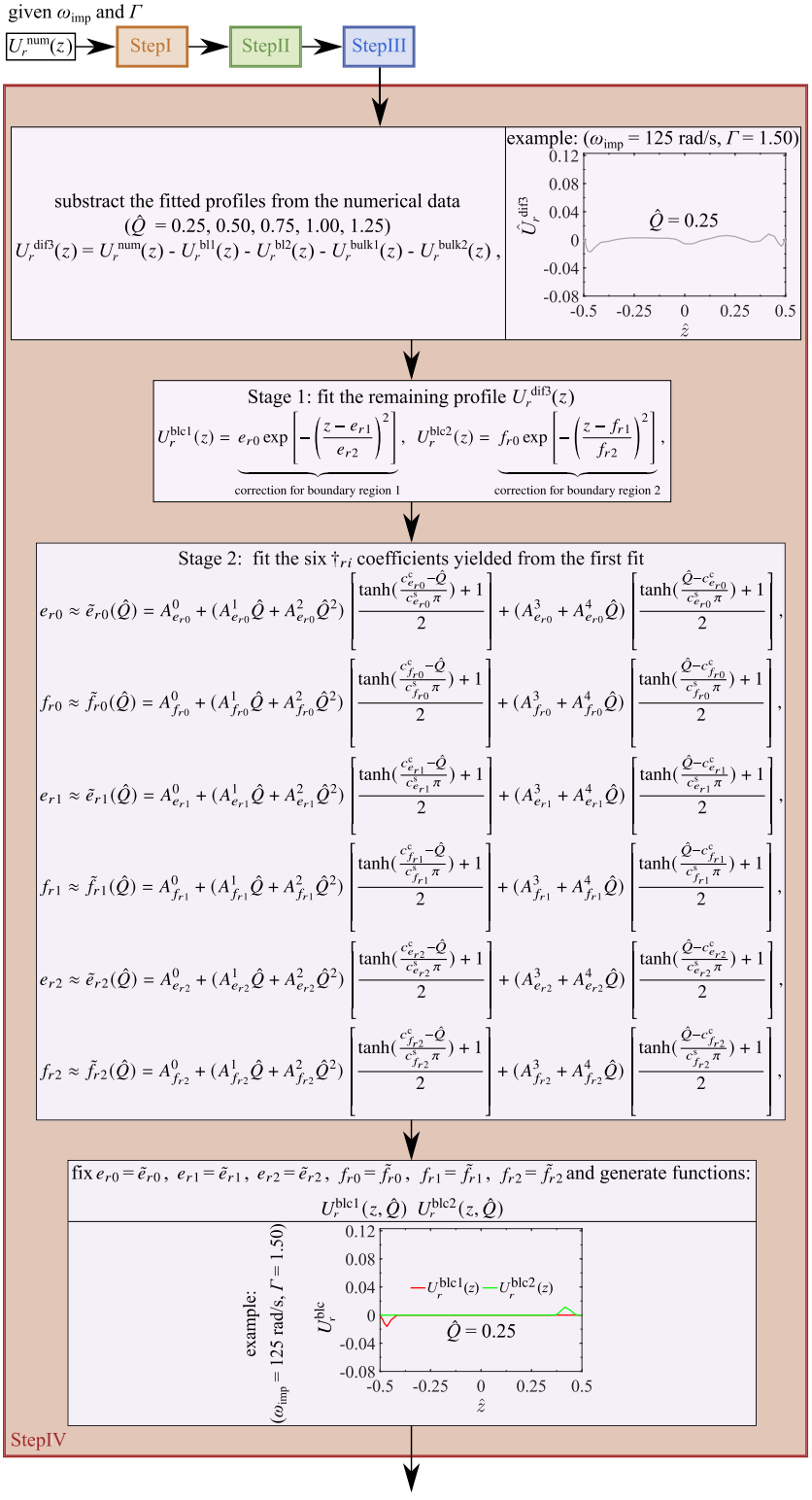

Fig. 9. Flowchart of the fourth fitting step for the radial velocity function. In output of this step we determine U_r^{blc1} and U_r^{blc2} as explicit functions.

$$U_r^{blc1}(z) = \underbrace{e_{r0}\exp\left[-\left(\frac{z-e_{r1}}{e_{r2}}\right)^2\right]}_{\text{correction for boundary region 1}}, \tag{11}$$

$$U_r^{blc2}(z) = \underbrace{f_{r0}\exp\left[-\left(\frac{z-f_{r1}}{f_{r2}}\right)^2\right]}_{\text{correction for boundary region 2}}, \tag{12}$$

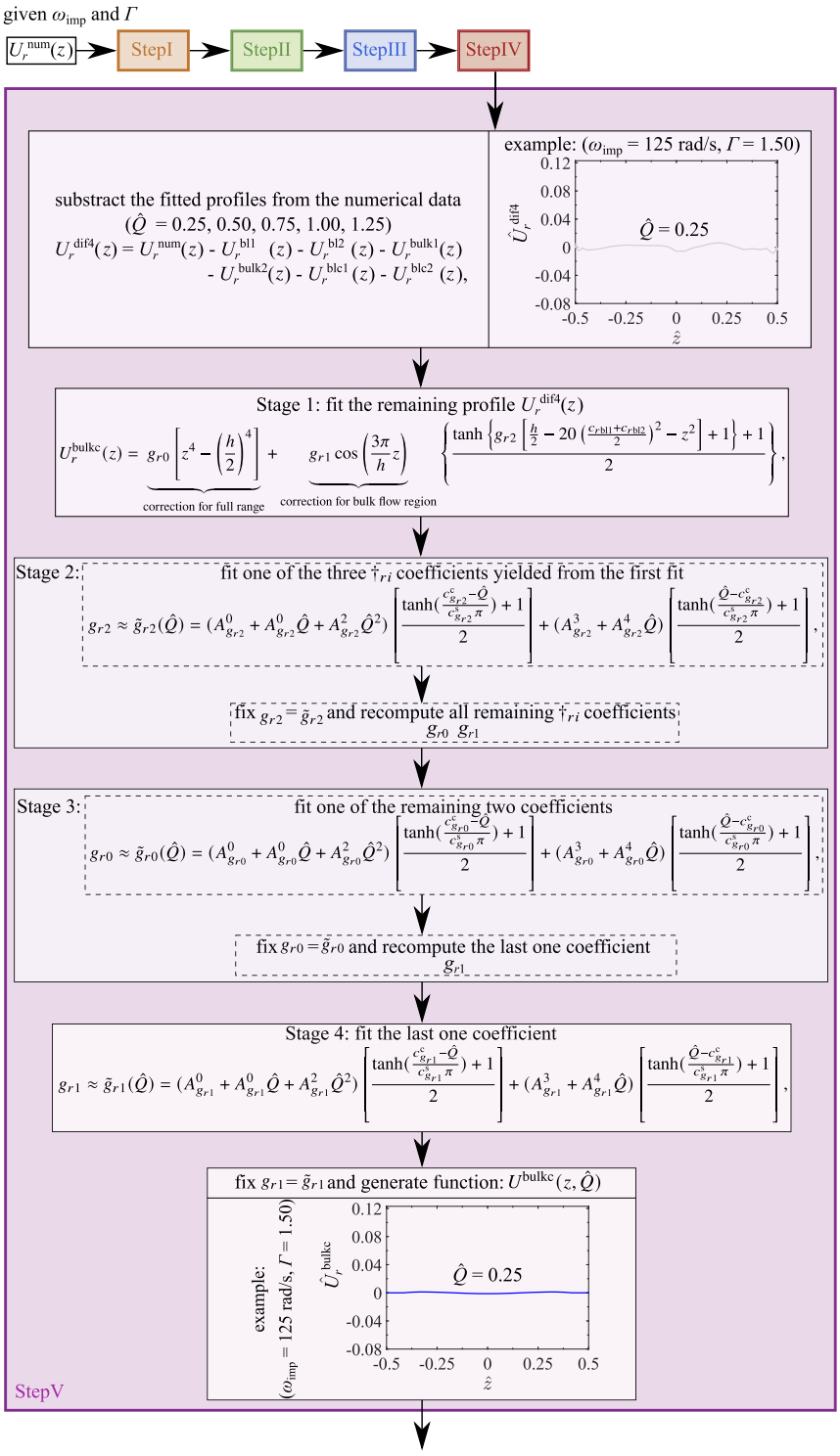

Fig. 10. Flowchart of the fifth fitting step for the radial velocity function. In output of this step we determine U_r^{bulkc} as an explicit function.

the fitting algorithm of this step is different from the others because all the $\dagger_{ri}$ coefficients are fitted in $\hat{Q}$ at the same time without employing four stages. As shown in Fig. 9, it consists of only two stages:

Stage 1. The six coefficients $\dagger_{ri}$ (where $\dagger \in \{e, f\}$, $i \in \{0, 1, 2\}$) in the first fit functions are determined by fitting the profile remaining from the previous three steps U_r^{dif3} for each triple $(\Gamma, \omega_{imp}, \hat{Q})$ with $\Gamma \in \{1.25, 1.50, 1.75, 2.00, 2.50\}$, $\omega_{imp} \in \{10, 40, 75, 125, 180\}$ rad/s and $\hat{Q} \in \{0.25, 0.50, 0.75, 1.00, 1.25\}$.

Stage 2. The six coefficients $\dagger_{ri}$ obtained in Stage 1 are updated by a secondary fit such that they depend on the flow rate $\hat{Q}$ (see Fig. 12). With all the coefficients $A^j_{\dagger_{ri}}$ yielded from secondary fitting, the functions $U_r^{blc1}(z, \hat{Q})$ and $U_r^{blc2}(z, \hat{Q})$ can be generated.

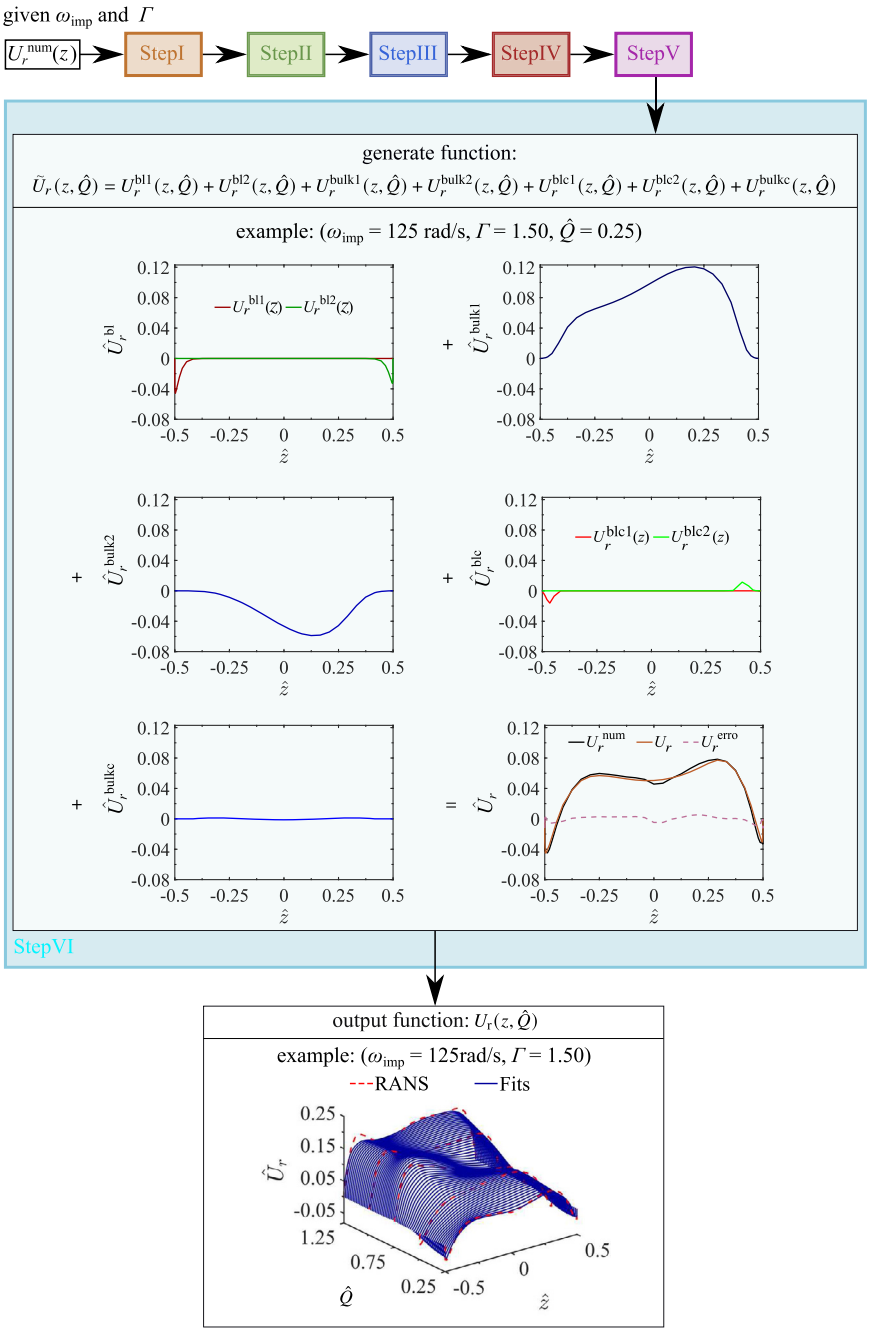

Fig. 11. Flowchart of the sixth fitting stage for the radial velocity function. In output of this step we determine $U_r(z,\hat{Q})$ as an explicit function.

Step V: corrects for the remaining bulk flow deviations by fitting the profile remaining from the previous four steps

$$U_r^{dif4}(z) = U_r^{num}(z) - U_r^{bl1}(z) - U_r^{bl2}(z) - U_r^{bulk1}(z) - U_r^{bulk2}(z) - U_r^{blc1}(z) - U_r^{blc2}(z), \tag{13}$$

using a fourth power function combined with a trigonometric function

$$U_r^{bulkc}(z) = \underbrace{g_{r0}\left[z^4 - \left(\frac{h}{2}\right)^4\right]}_{\text{correction for full range}} + \underbrace{g_{r1}\cos\left(\frac{3\pi}{h}z\right)}_{\text{correction for bulk flow region}} \left\{\frac{\tanh\left\{g_{r2}\left[\frac{h}{2} - 20\left(\frac{c_{rbl1}+c_{rbl2}}{2}\right)^2 - z^2\right] + 1\right\} + 1}{2}\right\}, \tag{14}$$

the fitting procedure of this step follows formally the same stages as in Step I, Step II, and Step III (see Fig. 10).

Step VI: sums all the fitted functions

$$\tilde{U}_r(z,\hat{Q}) = U_r^{bl1}(z,\hat{Q}) + U_r^{bl1}(z,\hat{Q}) + U_r^{bulk1}(z,\hat{Q}) + U_r^{bulk2}(z,\hat{Q}) + U_r^{blc1}(z,\hat{Q}) + U_r^{blc2}(z,\hat{Q}) + U_r^{bulkc}(z,\hat{Q}), \tag{15}$$

and then outputs the final function $\tilde{U}_r(z,\hat{Q})$ as explained in Fig. 11.

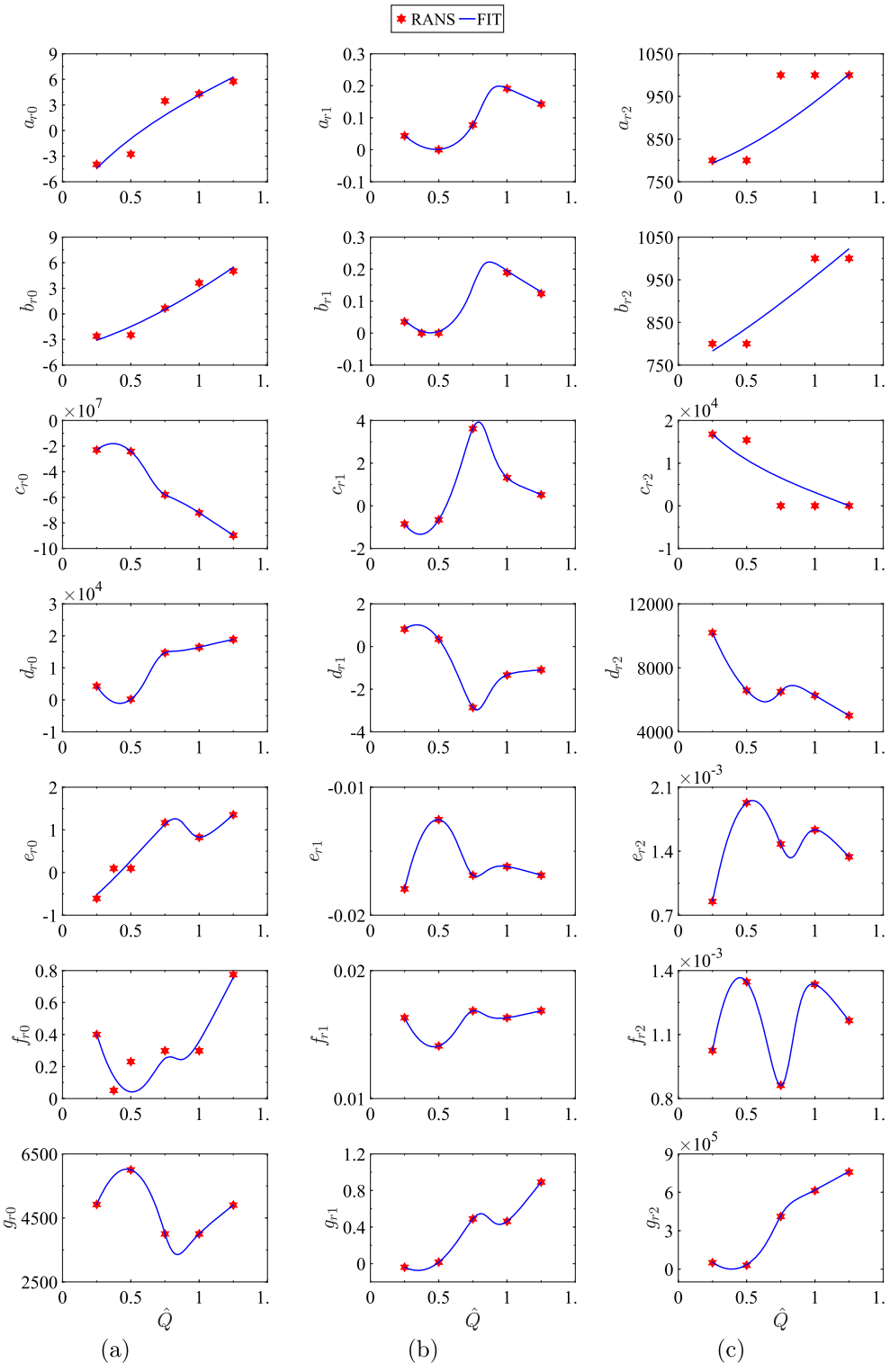

Fig. 12. Secondary fitting for the coefficients $\dagger_{ri}$ of U_r with the rotational speed $\omega_{\text{imp}} = 125$ rad/s and diffuser radius ratio $\Gamma = 1.50$ of the positive-leakage case.

Note the order of fitting the three coefficients $\dagger_{r0}$, $\dagger_{r1}$, and $\dagger_{r2}$ in each step is not fixed and depends on the specific case. The secondary fitting functions we adopted are based on the variation trend of the fitting coefficient $\dagger_{ri}$ with the flow rate $\hat{Q}$, the fitting results of the coefficients $\dagger_{ri}$ of U_r with the rotational speed $\omega_{\text{imp}} = 125$ rad/s and diffuser radius ratio $\Gamma = 1.50$ of the positive-leakage case is given in Fig. 12(a) as an example.

The same fitting procedure is applied for the tangential velocity $U_\theta(z)$ of the positive-leakage case. The fitting procedure is further adapted for the axial velocity $U_z(z)$ owing to the major topological differences of the profile to fit:

Step I: fits the bulk flow firstly using a quadratic function combined with a trigonometric function

$$U_z^{\mathrm{bulk1}}(z) = \underbrace{a_{z0}\left[z^2 - (\frac{h}{2})^2\right] + a_{z1}\cos\left(\frac{2\pi}{h}z + \frac{\pi}{2}\right)}_{\text{full range}}. \tag{16}$$

Step II: fits the bulk flow part remaining from Step I

$$U_z^{\mathrm{dif1}}(z) = U_z^{\mathrm{num}}(z) - U_z^{\mathrm{bulk1}}(z), \tag{17}$$

using a quadratic function combined with another trigonometric function

$$U_z^{\mathrm{bulk2}}(z) = \underbrace{b_{z0}\left[z^2 - (\frac{h}{2})^2\right] + b_{z1}\cos\left(\frac{4\pi}{h}z + \frac{\pi}{2}\right)}_{\text{full range}}. \tag{18}$$

Step III: fits the two boundary layer regions of the profile remaining from the previous two steps

$$U_z^{\mathrm{dif2}}(z) = U_z^{\mathrm{num}}(z) - U_z^{\mathrm{bulk1}}(z) - U_z^{\mathrm{bulk2}}(z), \tag{19}$$

using the power-law function

$$\begin{aligned} U_z^{\mathrm{bl1}}(z) &= \underbrace{c_{z0}\left(\frac{h}{2} + z\right)^{c_{z1}}}_{\text{boundary region 1}} \left\{\frac{\tanh\left[c_{z2}\left(c_{z\mathrm{bl1}} - \frac{h}{2} - z\right)\right] + 1}{2}\right\}, \\ U_z^{\mathrm{bl2}}(z) &= \underbrace{d_{z0}\left(\frac{h}{2} - z\right)^{d_{z1}}}_{\text{boundary region 2}} \left\{\frac{\tanh\left[d_{z2}\left(c_{z\mathrm{bl2}} - \frac{h}{2} - z\right)\right] + 1}{2}\right\}. \end{aligned} \tag{20}$$

Step IV: corrects for the remaining bulk flow deviations by fitting the profile remaining from the previous three steps

$$U_z^{\mathrm{dif3}}(z) = U_z^{\mathrm{num}}(z) - U_z^{\mathrm{bulk1}}(z) - U_z^{\mathrm{bulk2}}(z) - U_z^{\mathrm{bl1}}(z) - U_z^{\mathrm{bl2}}(z), \tag{21}$$

using a quadratic function combined with a trigonometric function

$$U_z^{\mathrm{bulkc}}(z) = \underbrace{e_{z0}\left[z^2 - (\frac{h}{2})^2\right] + e_{z1}\cos\left(\frac{4\pi}{h}z + \frac{\pi}{2}\right)}_{\text{full range}}. \tag{22}$$

Step V: sums all the fitted functions

$$\tilde{U}_z(z, \hat{Q}) = U_z^{\mathrm{bulk1}}(z, \hat{Q}) + U_z^{\mathrm{bulk2}}(z, \hat{Q}) + U_z^{\mathrm{bl1}}(z, \hat{Q}) + U_z^{\mathrm{bl2}}(z, \hat{Q}) + U_z^{\mathrm{bulkc}}(z, \hat{Q}), \tag{23}$$

and then outputs the final function $\tilde{U}_z(z, \hat{Q})$.

Owing to the lower leakage flow, for the zero- and negative-leakage case, the fitting is easier because the step to correct the boundary parts (see Fig. 9) for the radial U_r and tangential velocity U_θ are not needed anymore. The fitting method is flexible with adjustable orders of fitting steps adapt to different cases. Meanwhile, different combinations of different fitting functions are available. All the secondary fitting functions adopted for the coefficients $\dagger_{*i}$ (see Fig. 12) are reported below

$$\dagger_{*i}(\hat{Q}) = A^0_{\dagger_{*i}}, \tag{24a}$$

$$\dagger_{*i}(\hat{Q}) = A^0_{\dagger_{*i}}\hat{Q}^{A^1_{\dagger_{*i}}} + A^2_{\dagger_{*i}}, \tag{24b}$$

$$\dagger_{*i}(\hat{Q}) = A^0_{\dagger_{*i}}\hat{Q}^{A^1_{\dagger_{*i}}} + A^2_{\dagger_{*i}}\hat{Q} + A^3_{\dagger_{*i}}, \tag{24c}$$

$$\dagger_{*i}(\hat{Q}) = A^0_{\dagger_{*i}} + A^1_{\dagger_{*i}}\hat{Q}\left[\frac{\tanh(\frac{c^c_{\dagger_{*i}} - \hat{Q}}{c^s_{\dagger_{*i}}\pi}) + 1}{2}\right] + (A^2_{\dagger_{*i}} + A^3_{\dagger_{*i}}\hat{Q} + A^4_{\dagger_{*i}}\hat{Q}^2)\left[\frac{\tanh(\frac{\hat{Q} - c^c_{\dagger_{*i}}}{c^s_{\dagger_{*i}}\pi}) + 1}{2}\right], \tag{24d}$$

$$\dagger_{*i}(\hat{Q}) = (A^0_{\dagger_{*i}} + A^1_{\dagger_{*i}}\hat{Q})\left[\frac{\tanh(\frac{c^c_{\dagger_{*i}} - \hat{Q}}{c^s_{\dagger_{*i}}\pi}) + 1}{2}\right] + (A^2_{\dagger_{*i}} + A^3_{\dagger_{*i}}\hat{Q} + A^4_{\dagger_{*i}}\hat{Q}^2)\left[\frac{\tanh(\frac{\hat{Q} - c^c_{\dagger_{*i}}}{c^s_{\dagger_{*i}}\pi}) + 1}{2}\right], \tag{24e}$$

Table 2
Functions chosen for secondary fitting of the fitting coefficients $\dagger_{*i}$.

Func	$\dagger_{ri}$	$\dagger_{\theta i}$	$\dagger_{zi}$
positive-leakage case			
(24a)	/	a_2, b_2, d_2	/
(24b)	a_0, a_2, b_0, b_2	a_0, b_0	/
(24c)	c_2	c_2	/
(24d)	/	/	$c_0, c_1, c_2, d_0, d_1, d_2, e_0, e_1$
(24e)	/	/	a_0, a_1, b_0, b_1
(24f)	$a_1, b_1, e_0, e_1, e_2, f_0, f_1, f_2$	$a_1, b_1, e_0, e_1, e_2, f_0, f_1, f_2$	/
(24g)	d_1, d_2, g_0, g_1, g_2	d_1, g_0, g_1, g_2	/
(24h)	c_0, c_1, d_0	c_0, c_1, d_0	/
negative-leakage case			
(24c)	a_1, b_1, c_0	a_1, b_1, c_0	/
(24d)	/	/	$d_0, d_1, d_2, e_0, e_1, e_2$
(24e)	/	/	$a_0, a_1, b_0, b_1, c_0, c_1$
(24f)	a_0, a_2, b_0, b_2	a_0, a_2, b_0, b_2	/
(24g)	$c_1, c_2, d_0, d_1, e_0, e_1$	$c_1, c_2, d_0, d_1, e_0, e_1$	/
zero-leakage case			
(24c)	a_1, b_1, c_0	a_1, b_1, c_0	d_1, e_1
(24d)	/	/	d_0, d_2, e_0, e_2
(24e)	/	/	$a_0, a_1, b_0, b_1, c_0, c_1$
(24f)	$a_0, b_0, a_2, b_2, e_0, e_1$	$a_0, b_0, a_2, b_2, e_0, e_1$	/
(24g)	c_1, c_2, d_0, d_1, d_2	c_1, c_2, d_0, d_1, d_2	/

$$\dagger_{*i}(\hat{Q}) = A^0_{\dagger_{*i}} + (A^1_{\dagger_{*i}}\hat{Q} + A^2_{\dagger_{*i}}\hat{Q}^2)\left[\frac{\tanh(\frac{c^c_{\dagger_{*i}}-\hat{Q}}{c^s_{\dagger_{*i}}\pi})+1}{2}\right] + (A^3_{\dagger_{*i}} + A^4_{\dagger_{*i}}\hat{Q})\left[\frac{\tanh(\frac{\hat{Q}-c^c_{\dagger_{*i}}}{c^s_{\dagger_{*i}}\pi})+1}{2}\right], \tag{24f}$$

$$\dagger_{*i}(\hat{Q}) = (A^0_{\dagger_{*i}} + A^0_{\dagger_{*i}}\hat{Q} + A^2_{\dagger_{*i}}\hat{Q}^2)\left[\frac{\tanh(\frac{c^c_{\dagger_{*i}}-\hat{Q}}{c^s_{\dagger_{*i}}\pi})+1}{2}\right] + (A^3_{\dagger_{*i}} + A^4_{\dagger_{*i}}\hat{Q})\left[\frac{\tanh(\frac{\hat{Q}-c^c_{\dagger_{*i}}}{c^s_{\dagger_{*i}}\pi})+1}{2}\right], \tag{24g}$$

$$\dagger_{*i}(\hat{Q}) = (A^0_{\dagger_{*i}} + A^1_{\dagger_{*i}}\hat{Q} + A^2_{\dagger_{*i}}\hat{Q}^2)\left[\frac{\tanh(\frac{c^c_{\dagger_{*i}}-\hat{Q}}{c^s_{\dagger_{*i}}\pi})+1}{2}\right] + (A^3_{\dagger_{*i}}\hat{Q} + A^4_{\dagger_{*i}}\hat{Q}^2)\left[\frac{\tanh(\frac{\hat{Q}-c^c_{\dagger_{*i}}}{c^s_{\dagger_{*i}}\pi})+1}{2}\right], \tag{24h}$$

and the corresponding functions chosen for different cases are given in the Table 2. As a result of our fitting method, the three components of the velocity profile at the diffuser inlet are approximated as explicit functions of the flow rate $\hat{Q}$.

5. Results

5.1. Accuracy assessment

A comparison between the diffuser inlet velocity profiles determined numerically from the RANS simulation (solid line) and the profiles resulting from the above fitting procedure (dash line) is shown in Fig. 13 for three different leakage configurations with the rotational speed ω_{imp} = 125 rad/s and the diffuser radius ratio Γ = 1.50 at the flow rate Q/Q_d = 0.25, 0.50, 0.75, 1.00, and 1.25. For all cases, the simulated and fitted velocity profiles are in excellent agreement over the whole range of z. In addition, the error E of the fits is analyzed with respect to the original numerical data to fit. The normalized error of the radial velocity $\hat{E}_{U_r}$, tangential velocity $\hat{E}_{U_\theta}$ and axial velocity $\hat{E}_{U_z}$ is defined as

$$\hat{E}_{U_r}(z) = \frac{E_{U_r}(z)}{Q/S} = \frac{U_r^{\text{num}}(z) - U_r(z)}{Q/S}, \tag{25}$$

$$\hat{E}_{U_\theta}(z) = \frac{E_{U_\theta}(z)}{\omega_{\text{imp}}R_3} = \frac{U_\theta^{\text{num}}(z) - U_\theta(z)}{\omega_{\text{imp}}R_3}, \tag{26}$$

$$\hat{E}_{U_z}(z) = \frac{E_{U_z}(z)}{U_z^{\text{ref}}(z)} = \frac{U_z^{\text{num}}(z) - U_z(z)}{U_z^{\text{ref}}(z)}, \tag{27}$$

where the U_z^{Ref} is defined differently for different geometries as it depends on the leakage flow rate Q_{leak}. For the cases with leakage, we assume that the axial velocity is symmetric at the diffuser inlet in z direction

$$U_z^{\text{ref}} = \frac{Q_{\text{leak}}}{\pi(R_3{}^2 - R_2{}^2)} \simeq \int_0^{\max(z)} \frac{U_z dz}{H_3/2}. \tag{28}$$

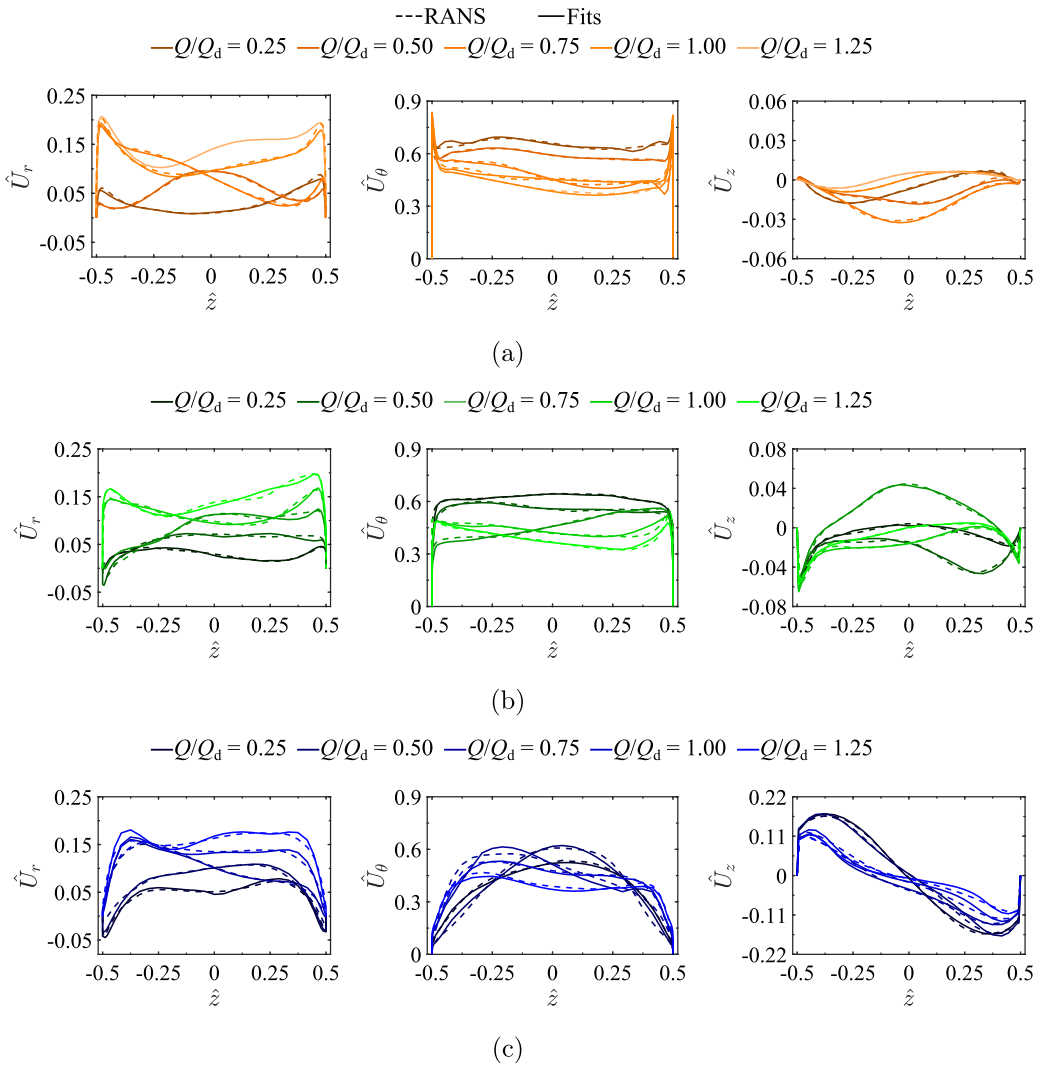

Fig. 13. Comparison of the diffuser inlet radial, tangential, and axial velocity profiles with the rotational speed $\omega_{\text{imp}} = 125$ rad/s and the diffuser radius ratio $\Gamma = 1.50$ obtained from the RANS simulation and the fitting of the three computational configurations: (a) zero-, (b) negative-, and (c) positive-leakage case.

For the zero-leakage case, the azimuthally-averaged two-dimensional continuity equation in cylindrical coordinates can be written as

$$\nabla_{rz} \cdot \vec{\bar{U}} = \frac{1}{r}\frac{\partial (r\bar{U}_r)}{\partial r} + \frac{\partial \bar{U}_z}{\partial z} = 0, \tag{29}$$

the parameters can be scaled as

$$r \sim R, \quad z \sim R\delta, \quad U_r \sim Q/S, \quad U_z \sim U_z^{\text{ref}}, \tag{30}$$

then the U_z^{ref} can be derived by balancing the order of magnitude of the two terms

$$\frac{Q}{SR} \sim \frac{U_z^{\text{ref}}}{R\delta} \Rightarrow U_z^{\text{ref}} = \frac{Q\,\delta}{S}. \tag{31}$$

The L2 norm of the scaled errors of the fitting is depicted in Fig. 14, which shows that the error norm is almost always below 15% for $\hat{U}_r$ and $\hat{U}_\theta$ with ω_{imp} = 125 rad/s and Γ = 1.50. The same statement holds true for all our other fits which constitute a clear assessment of accuracy for our fits. Keeping the L2-norm below 15% for $\hat{U}_r$ and $\hat{U}_\theta$ leads to a good quantitative agreement of the pressure and velocity fields when comparing the diffuser model supplemented by our scale-matching-fitted inlet against the full-pump simulations (see following sections for more details). This same condition is not respected when employing classic algebraic polynomial and Gaussian fits, whose performance at reproducing the full-pump results is poor (see Sec. 5.5 for a comparative study). The error on U_z is larger due to the sensitivity of U_z to the local leakage flow. Also in this case, the obtained accuracy is significantly higher than for traditional fitting techniques.

5.2. Inlet profile analysis

The diffuser performance correlates with the impeller outflow angle, non-uniformity, and unsteadiness of the inlet flow. The effect of flow rate Q and the impeller-diffuser leakage on diffuser inlet boundary conditions are discussed in this section. The fitted inlet velocity

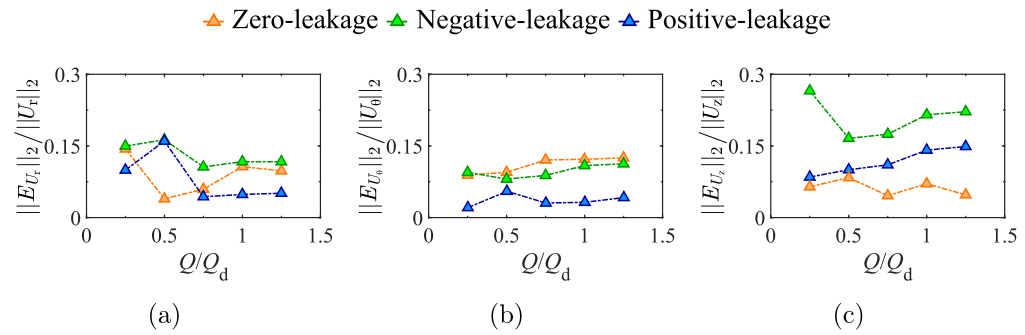

Fig. 14. Comparison of the fitting errors of (a) radial velocity, (b) tangential velocity, and (c) axial velocity for three different computational configurations with the rotational speed $\omega_{imp} = 125$ rad/s and the diffuser radius ratio $\Gamma = 1.50$.

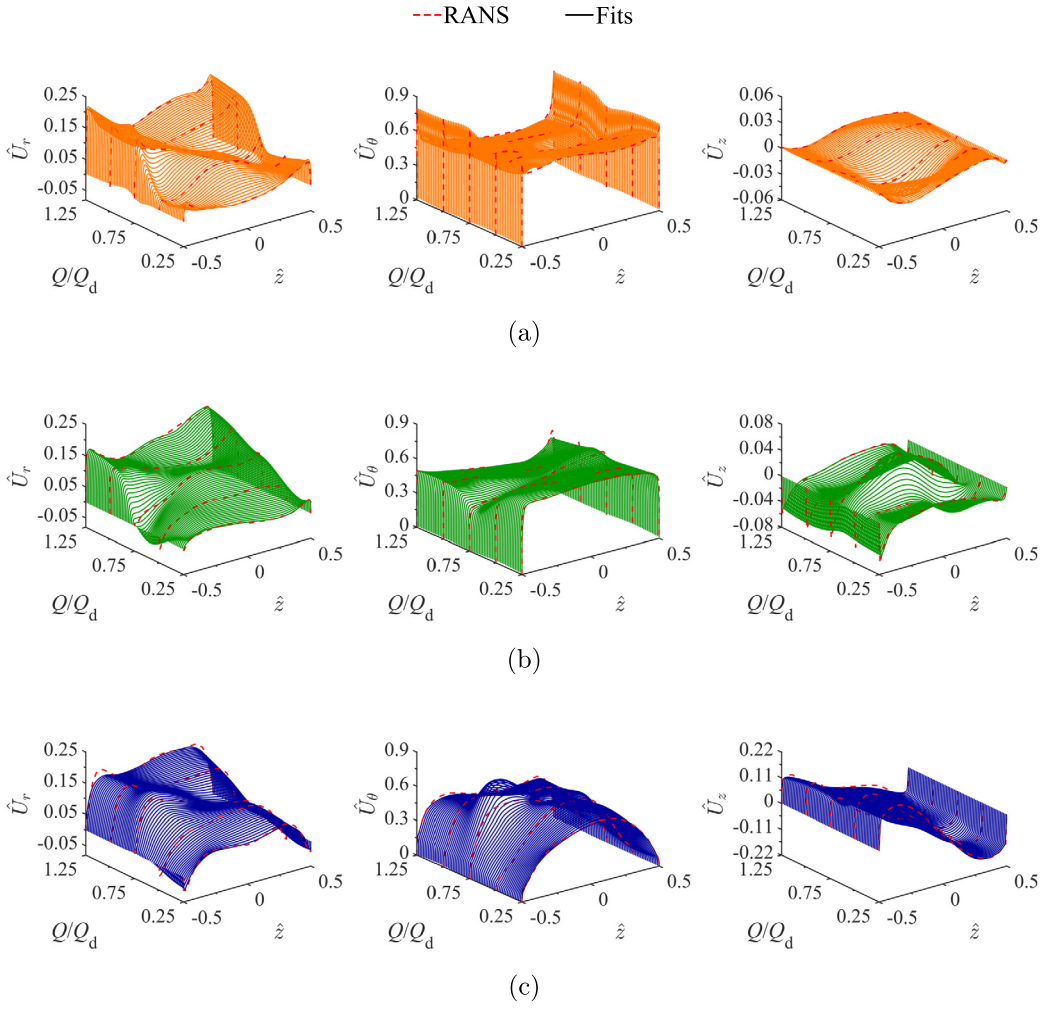

Fig. 15. Comparison of the fitted results of the radial, tangential, and axial velocity profiles with the rotational speed $\omega_{imp} = 125$ rad/s and the diffuser radius ratio $\Gamma = 1.50$ of the three different configurations: (a) zero-, (b) negative-, and (c) positive-leakage case.

profiles of three different leakage configurations with the rotational speed ω_{imp} = 125 rad/s and the diffuser radius ratio Γ = 1.50 are plotted in Fig. 15. The velocity profiles vary smoothly with the change of the flow rate Q.

For the zero-leakage case (see Fig. 15(a)), the radial velocity $\hat{U}_r$ decreased smoothly with the decrease of flow rate Q, and the boundary layer decayed rapidly after the flow rate Q/Q_d decreased below 0.75. The tangential velocity $\hat{U}_\theta$ and axial velocity $\hat{U}_z$ have some small fluctuations, and the amplitude of $\hat{U}_z$ is very low. Besides, we can observe that all the velocity profiles are almost symmetrically distributed in the z-direction over the whole range of flow rate Q except for $\hat{U}_z$ that must compensate for the continuity of mass.

For the negative-leakage case, the velocity profiles do not qualitatively change much compared with the zero-leakage case in $\hat{U}_r$ and $\hat{U}_\theta$. At the large flow rates, the radial velocity is more symmetrically distributed in z direction, but we can still find that the radial velocity near the shroud side is lower than the hub side, and the boundary layer decays much faster than the zero-leakage case. In fact, for this configuration, the pressure difference between the impeller outlet and the impeller inlet section leads to a leakage flow going out at the impeller-diffuser radial gap on the shroud wall, feeding back to the impeller inlet plane. This is the reason for the observed

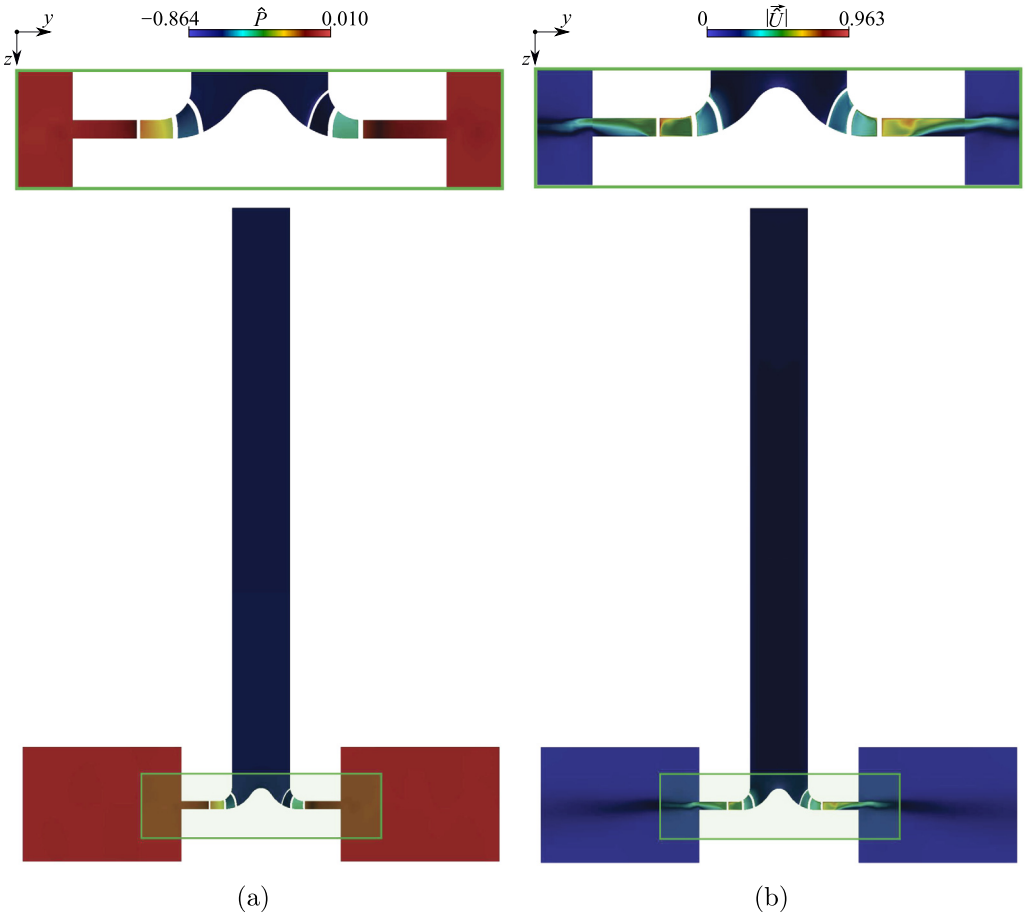

Fig. 16. Instantaneous color maps of the (a) static pressure and the (b) velocity magnitude at the mid-plane of the zero-leakage case of the centrifugal machine with the rotational speed $\omega_{\text{imp}} = 125$ rad/s and the diffuser radius ratio $\Gamma = 1.50$.

asymmetric. At small flow rates, the pressure difference between the impeller inlet and the outlet is larger, hence the velocity profiles are more asymmetrical. Moreover, the axial velocity $\hat{U}_z$ becomes more symmetric.

For the positive-leakage case, the leakage flow goes inside the vaneless diffuser, resulting in a larger boundary layer in $\hat{U}_r$ and $\hat{U}_\theta$. And the increased axial velocity magnitude $|\hat{U}_z|$ on both sides of the diffuser leads to an asymmetric $\hat{U}_z$. The large amplitude of $|\hat{U}_z|$ strongly perturbs the jet wake from the impeller.

Concerning the inlet profiles of the three different cases, we found that the leakage flow has a significant influence on the diffuser inlet boundary condition and leads to different instabilities characteristics which have been analyzed in Fan et al. [14].

5.3. Flow field analysis

For a better understanding of the flow field in the machine and the vaneless diffuser, the color maps of the zero-leakage case at the design condition $Q/Q_{\text{d}} = 1.00$ of the URANS results are shown first. The instantaneous static pressure p and velocity magnitude U_{mag} over the meridian section $x = 0$ are depicted in Fig. 16. The incompressible flow enters the centrifugal machine through the inlet pipe, very thin boundary layers develop in the inlet pipe (not clear at the scale of the color map) and a weak pressure gradient drives the flow down to the impeller. Once the flow reached the impeller, a strong tangential velocity component $\omega_{\text{imp}} r$ adds up to the flow velocity owing to the rotation of the impeller that channels the incoming flow through its blades. The rotating impeller imparts additional kinetic energy into the air stream by increasing the velocity of the air. The kinetic energy is then converted to increase the potential energy/static pressure by decelerating the flow through a vaneless diffuser. Meanwhile, it can be observed that the turbulent flow in the vaneless diffuser is asymmetric and highly skewed owing to the impingement on the hub and the boundary layer development on the diffuser walls.

To confirm that the simplified numerical model using the fitted diffuser inlet velocity profiles can reproduce the flow field inside the vaneless diffuser, the comparison of the azimuthally averaged color maps of the normalized instantaneous static pressure $\hat{p}$, radial $\hat{U}_r$, tangential $\hat{U}_\theta$, and axial velocity $\hat{U}_z$ at the design condition $Q/Q_{\text{d}} = 1.00$ of three different leakage configurations obtained from the RANS simulation of the whole machine model (up) and the simplified model (bottom) is shown in Fig. 17.

Note that for the simplified simulation, we employ the same numerical parameters of the experimentally validated RANS and URANS (see Fan et al. [15,14]). This being said, the simplified simulation with a circumferential-direction averaged velocity or with mimicked jet wakes is not aimed to exactly reproduce the inflow produced by the rotating impeller, but we rather want to reproduce its average flow and understand how this affects, all alone, the rotating instabilities. In fact, the major difference between the two unstable mechanisms observed in the vaneless diffuser is that the mechanism proposed by Tsujimoto et al. [5] only depends on the azimuthally-averaged flow, and the one proposed by Ljevar [8] relies on an azimuthally-modulated inflow. We aim to accurately reproduce the mean flow and then

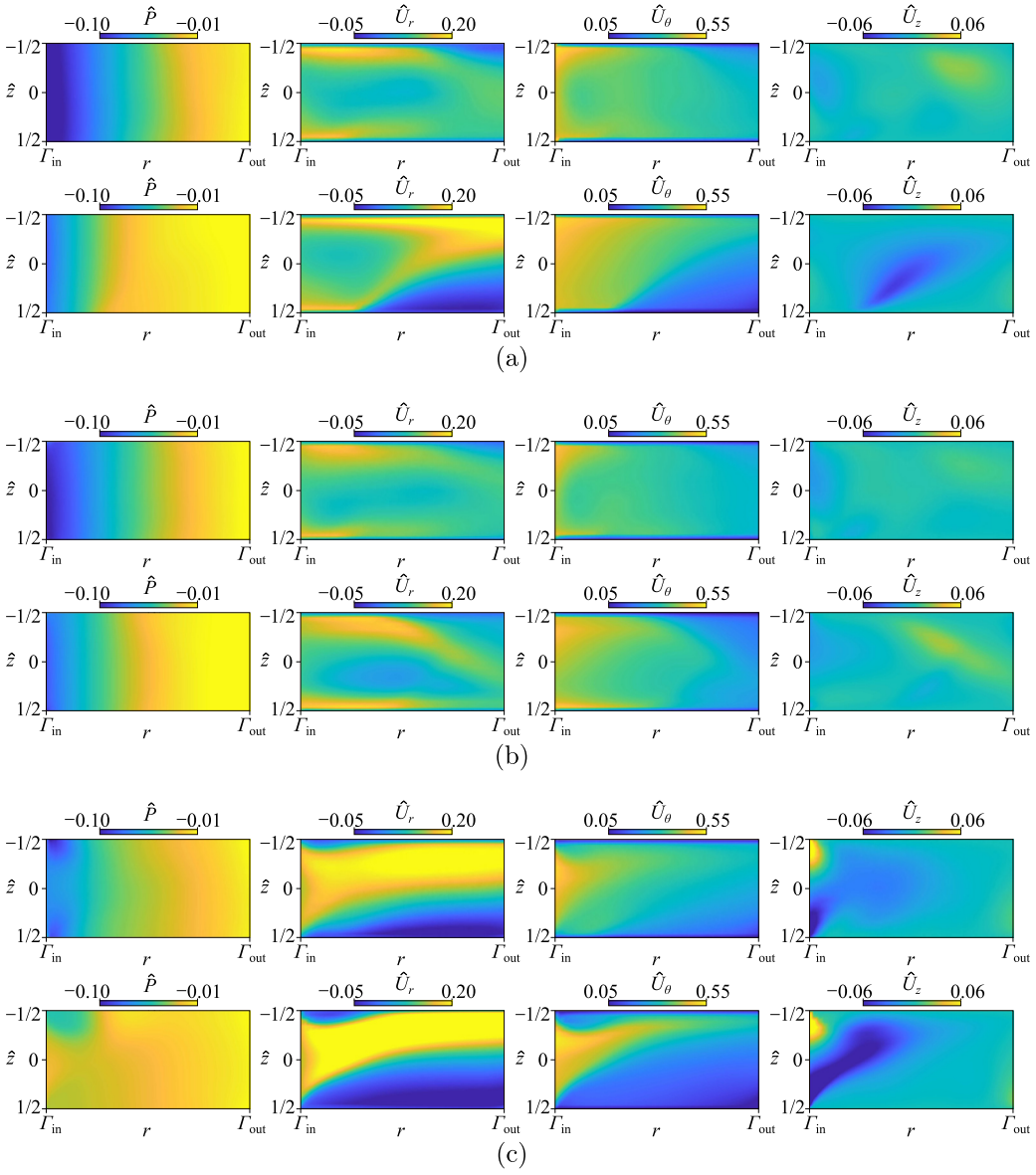

Fig. 17. Comparison of the azimuthally averaged colormaps of the static pressure, radial, tangential and axial velocity (from left to right) of RANS simulation of the entire machine (top), and RANS simulation for the diffuser only using our fit for the mean velocity profile as the inlet boundary condition (bottom) for the design flow rate $Q/Q_d = 1.00$ with the rotational speed ω_{imp} = 125 rad/s and radius ratio Γ = 1.50 for three different leakage configurations: (a) zero-, (b) negative-, and (c) positive-leakage case.

test azimuthal modulations in order to infer which instability mechanism holds in place upon the selected flow parameters. Hence, we do not aim to reproduce exactly the same flow field, but we rather want to build a model that will allow us to investigate in depth the nature of the vaneless diffuser instability keeping a certain consistency with real pump flows. Our results show that the flow field obtained from the simplified model is qualitatively matching and quantitatively close to the results obtained in the diffuser by simulating the whole machine but at 30% of the computational cost.

As the fitting protocol is relatively more accurate for $\hat{U}_r$ and $\hat{U}_\theta$ (see Fig. 14), the quantitative agreement between the colormaps for $\hat{U}_z$ is worse than for the other two velocity components. This also leads to a decrease of accuracy in terms of the pressure field, which, however, does not play an essential role if one aims to use the model for investigating the stability of the flow in the diffuser.

A significant difference between the model flow and the azimuthally-averaged diffuser velocity field of the RANS for the whole machine is however occurring for the zero-leakage case. In the following section, we will carry out a detailed investigation to explain why simulating the model flow leads to a remarkable boundary layer separation at the hub, which separation is not observed when simulating the whole machine.

5.4. Deviation of the mean flow field

As mentioned in the previous section, a significant deviation of the azimuthally-averaged flow field can be observed from the two simulations for the zero-leakage case. As shown in Fig. 17(a), a strong boundary layer separation occurs on the hub wall for the RANS results of the simplified model obtained using the mean flow profile at the inlet. As a consequence, such a separation leads to an ex-

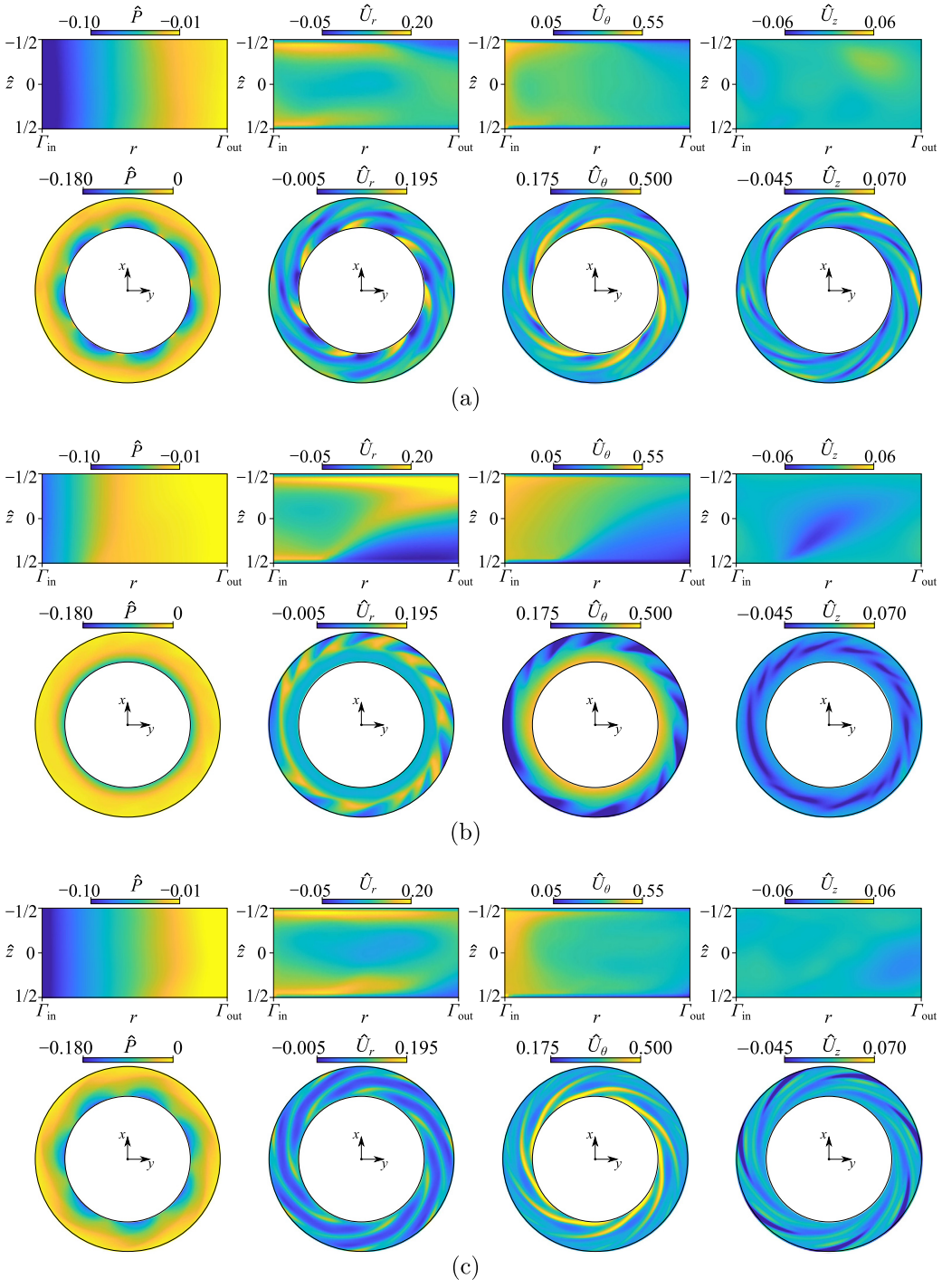

Fig. 18. Color maps of the instantaneous static pressure, radial velocity, tangential velocity, and axial velocity at the design condition $Q/Q_d = 1.00$ obtained by the RANS simulation for (a) the entire machine, (b) the simplified model with mean inlet flow, and (c) the simplified model with a approximately mimicked jet wake at the inlet. The upper figures display the azimuth-averaged value on the meridian section of the diffuser, while the lower figures show the instantaneous value at the mid-height of the diffuser.

tended mean backflow that can be observed near the diffuser outlet. A similar boundary layer separation is not found, however, in the azimuthally-averaged RANS results of the full machine.

To understand the origin of such a discrepancy, we first focus on the mid-height section of the vaneless diffuser. For the RANS of the whole machine, we can clearly identify the impeller jet wake at the inlet of the diffuser (see Fig. 18(a)). This same structure is not supposed to be present whenever simulating the model by enforcing an azimuthally-homogeneous inlet boundary condition. However, the bottom panels of Fig. 18(b) depict an azimuthally-periodic pattern that is typical of boundary layer instabilities. This could well explain why we found a boundary layer separation at the hub of the vaneless diffuser in our simplified diffuser model. We further stress that the instability pattern visible in Fig. 18(b) is confined to the separated region at the hub, which further points towards the diffuser instability as source of the observed discrepancy.

Building on these observations, we speculate that the discrepancies between the two flows are emerging because of the impact of the impeller jet wake that could stabilize the boundary layer. Hence, to test our conjecture, we carried out a new RANS simulation superposing a 7-periodic Fourier mode on the mean inlet profiles of the simplified model in order to approximately mimic the jet wake structure perturbation. The resulting inlet profile for the 7-periodic simplified model is

$$\hat{U}_r(\theta, z) = \tilde{U}_r(z) \cdot [1 + A\ \cos(m\theta)], \tag{32a}$$

$$\hat{U}_\theta(\theta, z) = \tilde{U}_\theta(z) \cdot [1 + A\ \sin(m\theta)], \tag{32b}$$

$$\hat{U}_z(\theta, z) = \tilde{U}_z(z) \cdot [1 + A\ \cos(m\theta)], \tag{32c}$$

where A denotes the amplitude of the perturbation, $m = 7$ denotes the wave number. We set the amplitude $A = 0.35$ which is matched to the amplitude of the tangential velocity of the jet wake for the impeller in full-machine simulations. The phase shift between radial and axial velocities ($\sim \cos(m\theta)$) compared to the tangential velocity ($\sim \sin(m\theta)$) is motivated by the single-Fourier mode continuity equation in cylindrical coordinates.

Fig. 18(c) shows the RANS results for the 7-periodic simplified model. The corresponding flow profile confirms our conjecture: The boundary layer instability that produces the separation at the hub (see Fig. 18(b)) is stabilized by the mimicked impeller jet wake (see Fig. 18(c)), where no major flow separations are observed. As a result, the simplified model with the 7-periodic inlet boundary condition is qualitatively and quantitatively very close to the RANS for the whole machine, which was the target of our model. This points toward the importance of reproducing the impeller jet wake, especially when no leakage flow is responsible for stabilizing the boundary layer in the vaneless diffuser. We further stress that, even if the jet wake produced by RANS results is not supposed to be an accurate approximation of a truly rotating impeller jet wake, its mean effect on the azimuthally-averaged flow is crucial. This points towards the importance of at least mimicking the jet wake (see (32)) whenever simplified inlet models, like ours, are used to reproduce the average inflow.

5.5. Comparison of fitting methods

The classic fitting methods used to approximate inflow profiles by algebraic polynomials or Gaussian functions are compared with our multi-stage fitting approach. To demonstrate the robustness of our scale-matching-like fitting technique, the velocity profiles of the zero-leakage case at the design flow rate are fitted with traditional one-stage fitting methods employing algebraic polynomials

$$\hat{U}_*(z) \approx \sum_{i=0}^{n} a_{*i}^P z^i, \tag{33}$$

and Gaussian functions

$$\hat{U}_*(z) \approx \sum_{i=1}^{n} a_{*i}^G \exp\left[-\left(\frac{z - b_{*i}^G}{c_{*i}^G} \right)^2 \right], \tag{34}$$

and then compared with our multi-stage fitting results, where a_i, b_i, and c_i denote the fitting coefficients, P and G are used for the polynomial and Gaussian fits, respectively, n denotes the degree of the polynomial functions or the number of Gaussian bells, and $*$ is either r, θ or z. The fitting results by algebraic polynomials functions for the radial velocity (see top panel of Fig. 19(a)) show that these fitting functions are too sensitive to the presence of boundary layers. Low-order fits do not capture the boundary layer, and higher-order fits introduce fictitious oscillations. The L2 norm of the error (see bottom panel of Fig. 19(a)) for our scale-matching fit is much lower than for the polynomial fits. Concerning the fitting results of the Gaussian functions (see top panel of Fig. 19(b)), the fit also introduces fictitious velocity profile oscillations. The corresponding L2 norm of the error (see bottom panel of Fig. 19(b)) shows that our scale-matching fit is more accurate.

Although implementing classic single-stage fitting functions is much easier and faster than using our method, this cheaper cost comes at the price of a significant reduction of accuracy and a number of numerical artifacts (namely a boundary condition discontinuity and a wavy profile). Our scale-matching fit does not suffer the nonphysical oscillatory artifacts introduced by polynomial and Gaussian functions. We do not see how such traditional single-stage fitting algorithms could reliably be used to supplement the sole diffuser flow in order to study the stability of the flow, which is affected by shear flow oscillations [18]. In fact, employing our scale-matching-like approach avoids the occurrence of such an artificial waviness in the fitted profile, hence increasing the reliability of our method over classic fitting protocols.

Our scale-matching is compared to classic fitting approaches in terms of their performance in reproducing the diffuser flow field velocity and pressure. The choice of the classic fits to compare with is motivated by three reasons: (i) algebraic polynomials of degree lower than 4 are excluded because they are not consistent with no-slip boundary conditions at the diffuser wall, (ii) 8th-degree polynomials maximize the robustness of the fit among the n that admit the minimum root-mean-square distance from the reference profile (see L2-norm in Fig. 19), and (iii) Gaussian fits for $n \geq 4$ are qualitatively capable of reproducing the boundary layer features of the inlet profile. Fig. 20 shows the azimuthally-averaged pressure and velocity components in the meridional plane for (a) the full pump simulations, (b) our scale-matching fit, (c) an 8-th degree polynomial fit, and (d) a Gaussian fit with 4 (top) and 8 (bottom) Gaussian bells. The scale-matching method proposed in this study correctly reproduces the pressure gradient, which is underestimated by polynomial and Gaussian fits. Moreover, whenever traditional methods are used, strong mean flow separation is observed on the hub wall (see the blue region in $\hat{U}_r$, $\hat{U}_\theta$, and $\hat{U}_z$) and the velocity at the shroud wall is over-predicted (see the yellow region in $\hat{U}_r$ and $\hat{U}_\theta$). The artifact of the mean flow separation is tamed down when our scale-matching approach is employed. Moreover, at the inlet of the diffuser, the waviness observed for the polynomial and Gaussian inlet-profile fits leads to the entrainment of a finger of azimuthal velocity in the bulk (see the wavy yellow region in Fig. 20(c,d)). This unphysical artifact is not present when using our scale-matching approach (see Fig. 20(b)), consistent with the corresponding full-pump simulations Fig. 20(a). Based on the above results, we can conclude that our scale-like matching fitting method performs significantly better than the classic fitting techniques we tested.

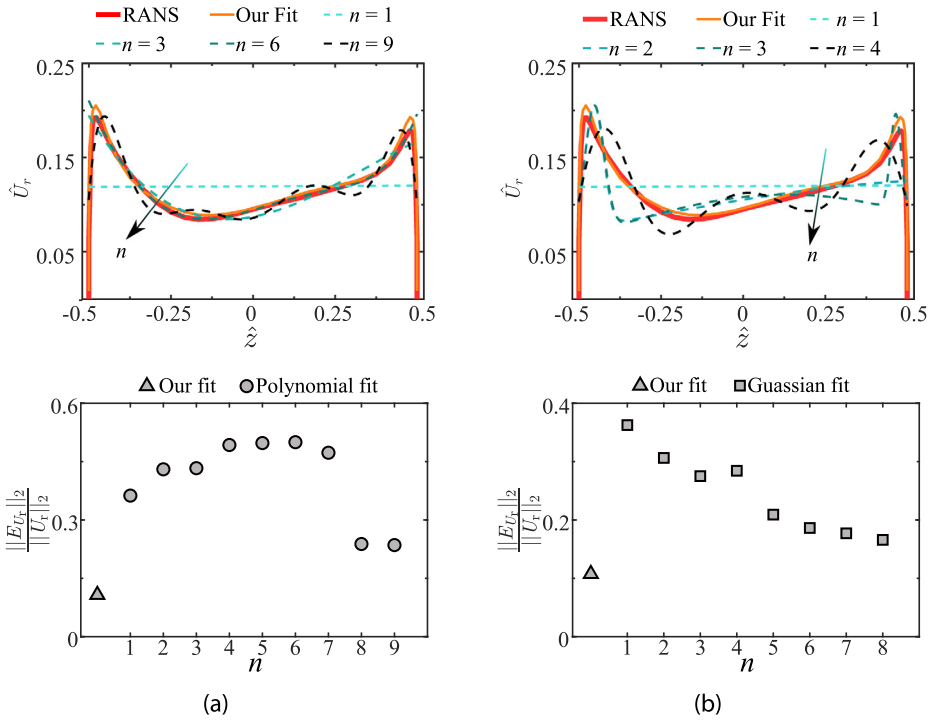

Fig. 19. Comparison between the radial velocity profiles U_r of the zero-leakage case at the design flow rate Q_d fitted by our multi-stage fitting method and (a) algebraic polynomials and (b) Gaussian functions.

5.6. Deviation of the diffuser performance

In order to evaluate the accuracy of the simplified model in predicting the diffuser performance, we define $\psi = \overline{p}_{\text{in}} - \overline{p}_{\text{out}}$, where $\overline{p}_{\text{in}}$ denotes the average pressure at the diffuser inlet and $\overline{p}_{\text{out}}$ the corresponding average pressure at the diffuser outlet. The relative error δ_r of the diffuser performance obtained by two different inflow conditions (average inflow with and without jet wake mimicked modulation) is depicted in Fig. 21. The relative error δ_r is calculated by

$$\delta_r = \left| \frac{\psi_{(\bullet)\text{ inflow,RANS}} - \psi_{\text{full machine, RANS}}}{\psi_{\text{full machine, RANS}}} \right|, \tag{35}$$

where $(\bullet)$ denotes either mean flow or mimicked jet wake inflow boundary condition.

The result shows that the relative error of diffuser performance obtained by the simplified model with the mean inflow condition is always larger than the result with the mimicked jet wake inflow condition. This further confirmed our previous conclusion that it is important to reproduce the impeller jet wake whenever simplified inlet models are used to reproduce the average inflow, otherwise numerical artifacts such as the mean flow separation at the hub could be induced by the inflow model (cf. Fig. 18(b,c)).

Concerning the results of the simplified case with the jet wake inflow condition, we find that the relative error of the zero-leakage case is very small. For the negative-leakage case, as we mentioned before, there is no leakage flow going inside the vaneless diffuser. The effect of leakage on the inlet velocity profiles is therefore of minor relevance. Hence, the relative error for this case remains small. For the positive-leakage case, the relative error of the jet wake inflow model increased but still remains below 20%, which is consistent with the accuracy of the mean flow profiles (see Fig. 14). The results show that our simplified model has limitations in reproducing the inflow condition when the jet wake entrains some fluid from an inlet radial gap before entering the diffuser. However, at a much lower computational cost and meshing complexity than the full-machine simulations, 20% of the performance deviation is considered acceptable.

5.7. Proof of principle

Finally, we want to prove that by just taking into account our fit to model the azimuthally averaged inlet profiles, we can successfully reproduce the low flow rate instability in the diffuser. To reproduce the rotating stall phenomenon at the small flow rate $Q/Q_d = 0.25$, an additional URANS simulation for the simplified model has been carried out for the zero-leakage case. A rotating inlet boundary condition is enforced in order to include the first harmonic produced by the impeller blades

$$\hat{U}_r(\theta, z, t) = \tilde{U}_r(z) \cdot \{1 + A \cdot \cos[(\theta - \omega_{\text{imp}} t) \cdot m]\}, \tag{36a}$$

$$\hat{U}_\theta(\theta, z, t) = \tilde{U}_\theta(z) \cdot \{1 + A \cdot \sin[(\theta - \omega_{\text{imp}} t) \cdot m]\}, \tag{36b}$$

$$\hat{U}_z(\theta, z, t) = \tilde{U}_z(z) \cdot \{1 + A \cdot \cos[(\theta - \omega_{\text{imp}} t) \cdot m]\}. \tag{36c}$$

The simulation results obtained from the simplified model that considers the sole diffuser are compared hereinafter with the corresponding vaneless diffuser when the entire machine is simulated.

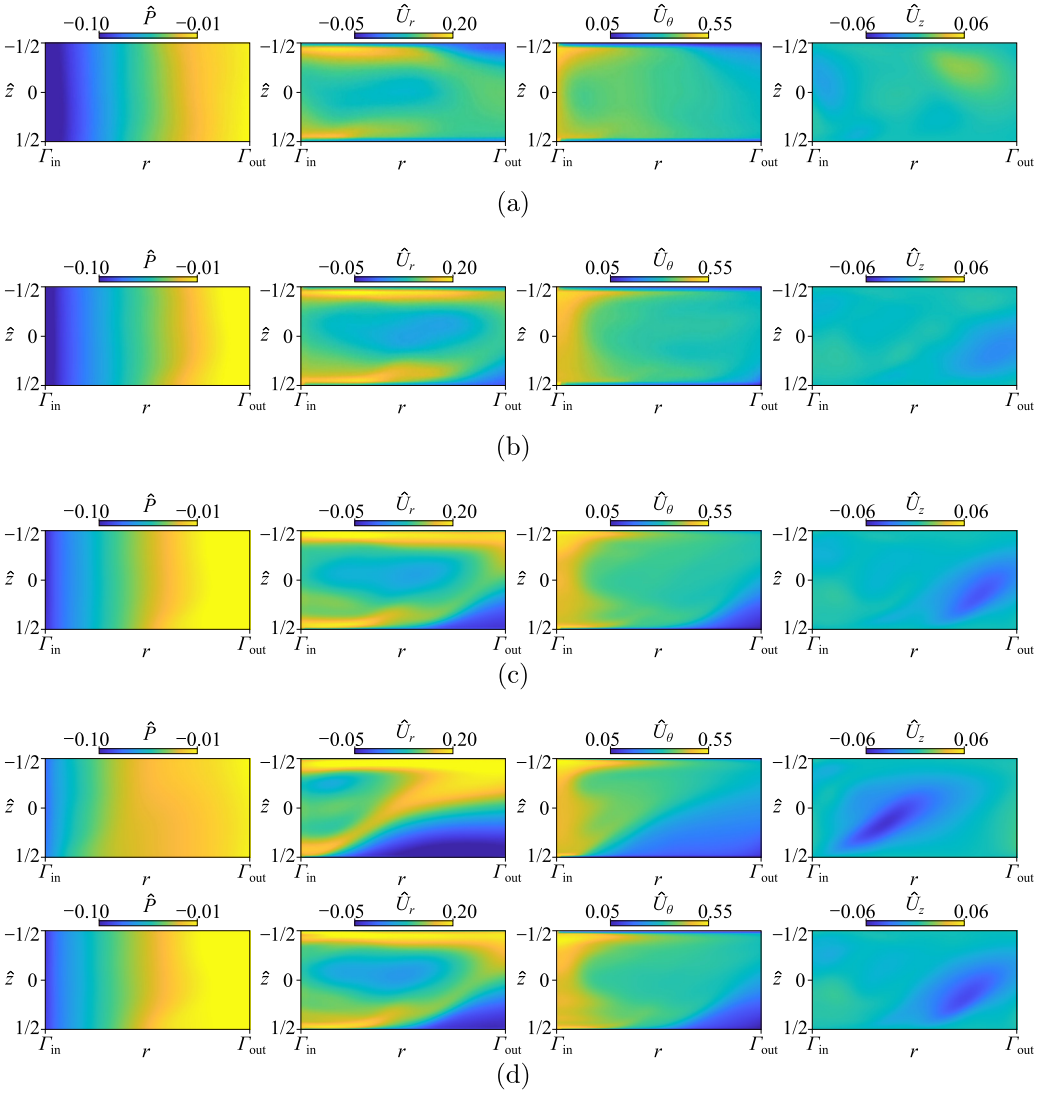

Fig. 20. Comparison of the azimuthally-averaged colormaps of the static pressure, radial, tangential, and axial velocity (from left to right) of RANS simulation for the design flow rate Q_d of (a) the entire machine and of the diffuser only using inlet mean velocity profiles fitted with different approaches: (b) our scale-like matching fit, (c) $n = 8$ polynomial fit, and (d) $n = 4$ (top) and $n = 8$ (bottom) Gaussian fits.

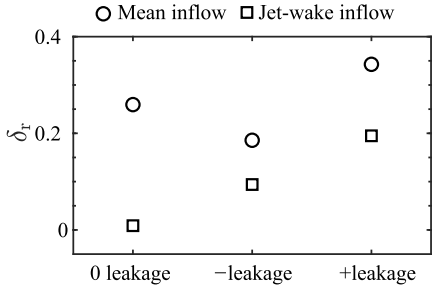

Fig. 21. Relative error δ_r of the diffuser performance predicted by the simplified model with two different inflow boundary conditions.

A Fourier decomposition analysis of the cross-power spectrum is conducted using the URANS simulation results from two numerical probes situated at the mid-radial distance of the diffuser shroud wall, with an angular phase shift of 60°, and verified against the experimental results. This analysis of the cross-power spectra of two pressure probes located at the same radius but at different angular positions enables the detection of rotating phenomena [20,21] and determines their characteristics, including the number of cells and propagation velocity.

The cross-power spectrum of the experiment at fully-developed stall condition Q/Q_d = 0.26 is shown on top of Fig. 22(a). As anticipated, the blade-passing-to-impeller-frequency ratio $f_{blade}/f_{imp} = 7$ is prominently visible in the cross-power spectrum, where f_{blade} and f_{imp} denotes the blade passing and impeller frequency, respectively. Moreover, a frequency associated with the low-flow-rate rotating stall $f_{stall,0.26Q_d}/f_{imp} = 0.840$ is detected. The FFT identifies therefore the propagation velocity of the stall cells $\omega_{stall,0.26Q_d} = 0.28\omega_{imp}$. Besides,

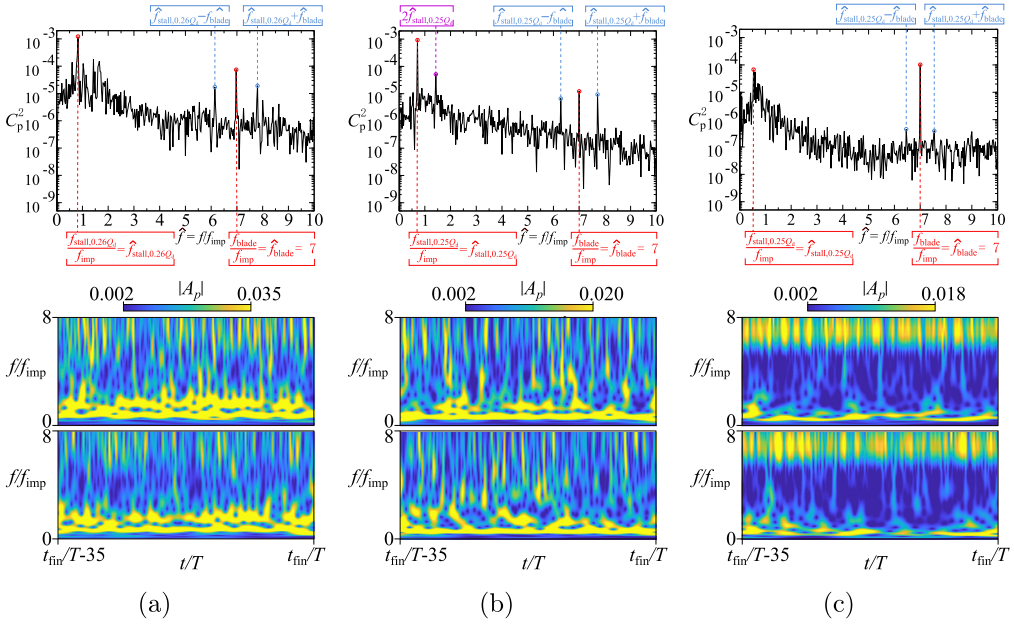

Fig. 22. Fourier and wavelet analysis of (a) the experiment and URANS simulation results of the zero-leakage case for (b) the whole machine and (c) the sole diffuser model at stalled condition.

the non-linear interaction between such two frequencies is also observed in the FFT at $f_{\text{stall},0.26Q_d} - f_{\text{imp}}$ and $f_{\text{stall},0.26Q_d} + f_{\text{imp}}$. As shown at the bottom of Fig. 22(a), the wavelet analysis confirms the presence of the rotating stall frequency, which is clearly identifiable. The complex energy transfer is visible for the frequencies near $f_{\text{stall},0.26Q_d}$. For the numerical results of the zero-leakage case at fully-developed stall condition $Q/Q_d = 0.25$ obtained from the entire machine, the blade-passing-to-impeller-frequency ratio $f_{\text{blade}}/f_{\text{imp}} = 7$, low-flow-rate rotating stall frequency $f_{\text{stall},0.25Q_d}/f_{\text{imp}} = 0.714$, and the non-linear interaction between such two frequencies $f_{\text{stall},0.25Q_d} - f_{\text{imp}}$ and $f_{\text{stall},0.25Q_d} + f_{\text{imp}}$ also can be clearly identified from the cross-power spectrum (see the top panel of Fig. 22(b)). The wavelet result shows good consistency with the FFT result. And the propagation velocity of the stall cells is identified as $\omega_{\text{stall},0.25Q_d} = 0.238\omega_{\text{imp}}$, which is quantitatively very close to the experimental result.

Fig. 22(c) shows the cross-power spectrum and wavelet analysis results obtained from the simplified model. The rotating stall frequency $\tilde{f}_{\text{stall},0.25Q_d}/f_{\text{imp}} = 0.543$, blade passing frequency $f_{\text{blade}}/f_{\text{imp}} = 7$, and the non-linear interaction between these two frequencies can be identified very clearly in FFT results (see the top of Fig. 22(c)). The FFT identifies therefore the propagation velocity of the stall cells $\tilde{\omega}_{\text{stall},0.25Q_d} = 0.181\omega_{\text{imp}}$, which underpredicts $\omega_{\text{stall},0.25Q_d}/\omega_{\text{imp}}$ of the whole machine. Both, the rotating stall frequency and the blade passing frequency, can be easily identified by the wavelet analysis as shown at the bottom of Fig. 22(c), and the complex non-linear transport of energy at $f \approx f_{\text{stall},0.25Q_d}$ is also qualitatively reproduced by the model. However, as we simplify the impeller jet wake to its first Fourier mode, the mid-range frequency interactions are weaker for the model flow (cf. Fig. 22(b,c)). Compared with the entire machine results, the amplitude of the rotating stall frequency is lower, and the blade passing frequency is higher. This is expected to occur also because of the single-Fourier-mode driving imposed at the inlet, which is less prone to induce non-linear interactions. Nevertheless, our simplified model captures all relevant features of the low-flow-rate instability, reducing the URANS simulation cost of 70%.

This is further confirmed by Fig. 23, which presents the comparison with the color maps of the PIV phase-averaged measurements of Dazin et al. [19] (Fig. 23(a), see Appendix B for more details) and numerical simulation for the entire machine Fig. 23(b) and for the simplified model Fig. 23(c) with 120-time steps of the last revolution at the mid-height of the diffuser in a reference frame rotating with the stall cell propagation velocity $\omega_{\text{stall},0.25Q_d}$ ($\tilde{\omega}_{\text{stall},0.25Q_d}$ for the model). Regarding the results, three stall cells can be observed in the two URANS simulations with a good qualitative agreement in comparison to the corresponding experiment. This means that the rotating stall phenomenon can be reproduced by the simplified simulation approach. From a quantitative point of view, the URANS simulation results of the entire machine are closer to the PIV result. The simulation results here are for the zero leakage case, whereas there is an impeller-to-diffuser gap in the PIV experiment. This leads to quantitative deviations in the tangential velocity distribution. For the URANS simulation of the sole diffuser, the quantitative deviation of the flow field is expectedly larger since only a single Fourier mode is simulated at the inlet in the circumferential direction. We further stress that our aim is to demonstrate that taking our reduced-order simulation approach can reproduce the typical rotational stall instability in a vaneless diffuser, rather than reproducing exactly the same flow field. In fact, our future studies will aim to simulate slightly supercritical conditions for which the instability will admit a much lower amplitude than the one depicted in Fig. 23. By employing our reduced-order modeling approach, the effect of blade numbers and characteristic features of the impeller jet wake can be investigated not too far from critical conditions.

6. Discussion and conclusions

This paper documents a simplified approach for the instabilities identification based on a new centrifugal 3D impeller outflow model. The three-dimensional model pays attention to the multiscale inlet boundary conditions at the impeller outlet plane including non-uniform flow close to reality, which is typically ignored in model simplification for vaneless diffusers. A detailed step-by-step method for fitting the diffuser inlet profiles in a centrifugal machine is documented.

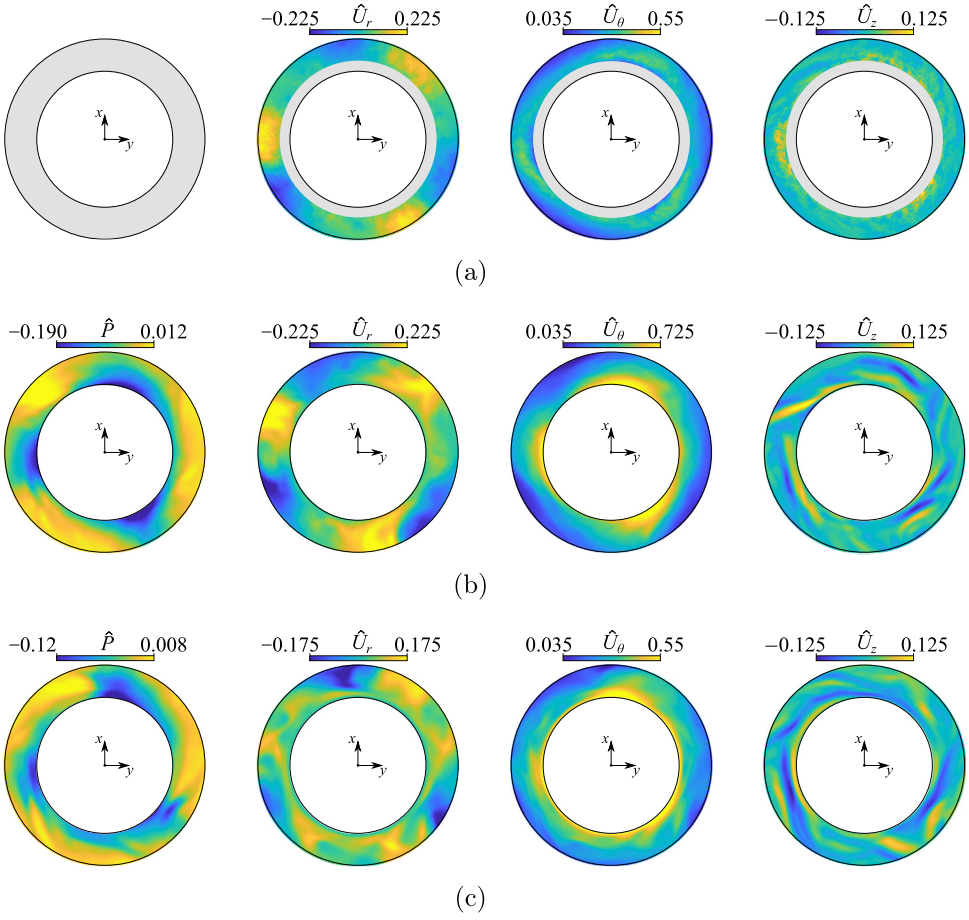

Fig. 23. Color maps of (a) the PIV phase-average measurements of Dazin et al. [19] and phase-average of the URANS simulation results for the zero leakage case for (b) the entire machine and (c) the simplified model at the stalled conditions. Due to laser reflection on the impeller blades, PIV cannot access the grey region near the diffuser inlet. Therefore, the measurements taken near the edge of this region should be regarded as having a significant margin of error.

The fitting results are close to the numerical simulation results, with the L2 norm of the errors being in an acceptable range. The flow field in the vaneless diffuser can be reproduced well by numerical simulation for the simplified model with the fitted inlet velocity profiles.

By superposing a periodic wave (with the wave number and amplitude corresponding to the jet wake from the impeller) to the mean inlet velocity profiles, URANS simulation in the simplified model can also reproduce the main features of the rotating stall instability in the diffuser at 30% of the total cost. The rotating instability phenomenon that occurs in the vaneless diffuser is affected by the leakage configuration via the inlet profile. However, how the boundary layer interacts with the instability mechanism is still not clear, which needs to be further studied.

At a much lower computational cost than the full-machine URANS simulations, the advantage of using our model is therefore that it can be employed to carry out cost-affordable parametric studies in which, not only we can vary the machine parameters such as flow rate Q, rational velocity ω_{imp}, diffuser radius ratio Γ, and different leakage configurations, but we can also investigate the effect of the number of blades and characteristic features of the impeller jet wake.

There are a few literature studies focused on this subject. Therefore, this work can provide some guidance for similar problems, that require a reduction of the computational cost. It is expected that the fitted inlet flow profile in the diffuser with the simplified numerical model can be useful to understand the different instability patterns and could also be used as a boundary condition for fundamental studies like linear stability analysis in the sole diffuser.

Declaration of competing interest

The authors declare the following financial interests/personal relationships which may be considered as potential competing interests:

Meng FAN reports financial support was provided by China Scholarship Council. Francesco ROMANO reports equipment, drugs, or supplies was provided by Grand Équipement National De Calcul Intensif.

Data availability

Data will be made available on request.

Acknowledgements

We kindly acknowledge the GENCI (grand équipement national de calcul intensif) for the numerical resources granted to conduct this study under project A0102A01741. Furthermore, we appreciate the support of the China Scholarship Council for the doctoral students of M. Fan (CSC student number 201908320328).

Appendix A. Evaluation of local Mach number

For the centrifugal machine we studied, the impeller tip velocity, which determines the maximum velocity in the centrifugal machine, is about 32 m/s, corresponding to a Mach number of about 0.1 which is safely lower than 0.3. To better justify the choice of incompressible Navier-Stokes equations, we now further employ simulations that include the whole pump to evaluate the Mach number throughout our simulation. Fig. A.24 depicts five color maps of the local Mach number at different instants on a longitudinal section (zoom in on the region of the impeller). They demonstrate the Mach number throughout the simulations is less than 0.3.

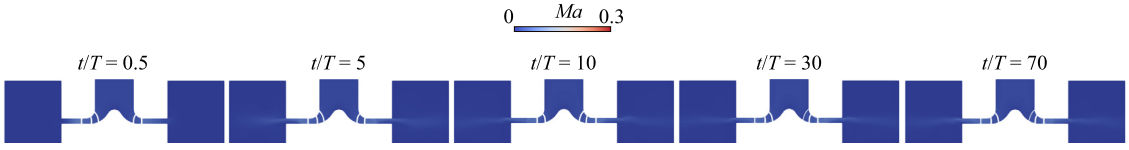

Fig. A.24. Color maps of the Mach number at the meridional section of the entire machine at the design condition Q_d at different simulation times.

Appendix B. Experimental apparatus

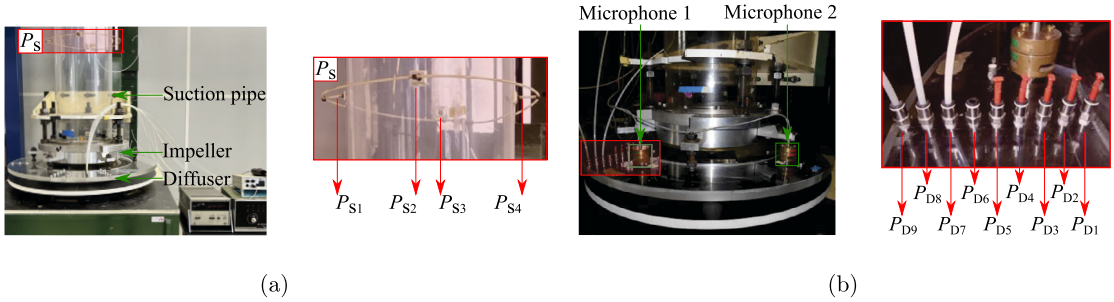

Fig. B.25. Experimental set-ups of the radial flow machine with (a) a zoom-in view of the four static pressure probes equipped on the suction pipe (red rectangle) and (b) two microphones and a zoom-in view of nine static pressure taps installed on the vaneless diffuser (red rectangle).

The experimental set-up including a radial impeller coupled with a vaneless diffuser is depicted in Fig. B.25 as already presented in previous works [14,15,19]. This arrangement allows positive leakage flow into the vaneless diffuser inlet due to the radial gap between the outlet rotating impeller section and the fixed inlet diffuser section. The inflow condition is given by a tank, equipped with a honeycomb flow straightener placed on the top of the suction pipe. The flow rate Q can be adjusted by a set of changeable diaphragms (with different radii) installed at the tank inlet.

The static pressure variation between the suction pipe (P_s) and impeller outlet is measured to determine the entire machine's performance. The suction pipe is equipped with four steady pressure probes as depicted in Fig. B.25(a), and the static pressure in the suction pipe is calculated as the average of four positions ($P_{s1} - P_{s4}$). In addition, nine steady pressure taps are radially and equally spaced on the diffuser wall (see Fig. B.25(b)). Therefore, the diffuser performance in terms of pressure recovery from the inlet to the diffuser outlet can be characterized. It is estimated that there is a margin of uncertainty of ± 2 Pa in these measurements. To detect the instabilities occurring in the vaneless diffuser, two Brüel & Kjaer (Nærum, Denmark) condenser micro-phones (Type 4135) were employed to measure the unsteady pressure fluctuation. The probes are positioned at the same radial distance of $r = 320$ mm on the diffuser wall, but with a relative angular displacement of $\Delta\theta = 60°$. The measurement uncertainty of these probes is less than 1%. Data was collected using LMS Test Xpress (SIEMENS, Munich, Germany) for a total duration of 600 s, with a sampling frequency of 4096 Hz.

The experiments were conducted in air, covering a wide range of flow rate ratios relative to the design condition, with Q/Q_d ranging from 0.26 to 1.53. Here, Q and Q_d represent the actual and design flow rates, respectively, and were measured at the inlet pipe with a constant rotating speed of $N = 1200$ rpm (i.e. $\omega_{imp} = 125$ rad/s).

The measurements of Dazin et al. [19] reported in Fig. 23 result from a 2D/3C high-repetition-rate PIV. Particles of incense smoke, which are smaller than 1 µm, were employed for seeding. Spectral analysis, both linear and non-linear, was employed to examine and categorize the unsteady phenomena within the signals. Subsequently, a specialized phase-averaging method was devised to effectively track and visualize the evolution of instabilities. A dedicated PIV averaging protocol was applied to the PIV flow fields such to capture and visualize the topology of the spectrally identified phenomena. The PIV results have been interpolated to a new mesh and then phase averaged during the acquisition process. As the interrogation window is fixed and the flow is rotating in the laboratory reference frame,

the experimental output consists of an ensemble of measurements that leads to the phase-averaged velocity components reproduced in dimensionless form in Fig. 23.

More detailed descriptions of the experimental measurements, data acquisition, and adopted pump operating points can be found in previous papers [15,19,22–25] that operate the same apparatus.

Appendix C. Grid independence analysis

Table C.3
Grid independence verification. The relative error, δ, is calculated with respect to the finest grid (denoted by Case 4), and is given by the equation: $\delta = |\text{PSICase 4} - \text{PSICase }^*|/|\text{PSI}_{\text{Case 4}}|$. Here, PSI represents the mass-weighted average static pressure difference between the inlet of the pipe and the outlet of the diffuser, and the asterisk denotes either Grid 1, Grid 2, or Grid 3.

Grid #	Cells number					PSI	δ
	inlet pipe	impeller	diffuser	outflow box	total		
1	113155	267008	145728	91800	617691	0.3843	1.75%
2	238853	493920	210600	175446	1118819	0.3864	2.30%
3	406462	1051176	590976	267786	2316400	0.3742	0.93%
4	1218825	2456160	1379448	352350	5406783	0.3777	–

To ensure grid independence, four different grid resolutions were tested in our study. Table C.3 compares the mass-weighted average static pressure difference between the inlet of the pipe and the outlet of the diffuser (PSI) predicted by each grid at the design condition. As the grid resolution increases from 618k cells (Grid 1) to approximately 1.1M cells (Grid 2), the relative error in predicting the machine performance also increases. However, the error decreases for 2.3M cells (Grid 3) and reaches a minimum of 0.93%. Therefore, a total mesh of 2.3M finite volumes was selected for the numerical simulations. Besides, to ensure the robustness of the flow to the mesh resolution in the boundary layer, we tested three different mesh stretchings, namely: (i) 13 wall layers with expansion ratios of 1.4, (ii) 11 wall layers with expansion ratios of 1.5, and (iii) 10 wall layers with expansion ratios of 1.6. The simulation results depicted in Fig. C.26 show that the flow in our setup is not very sensitive to the mesh stretching near the wall. Hence, all the conclusions of this study can safely be considered robust upon a change in the wall mesh refinement. Fig. C.26 further justifies our choice of using an expansion ratio of 1.5 for all the results presented in this paper.

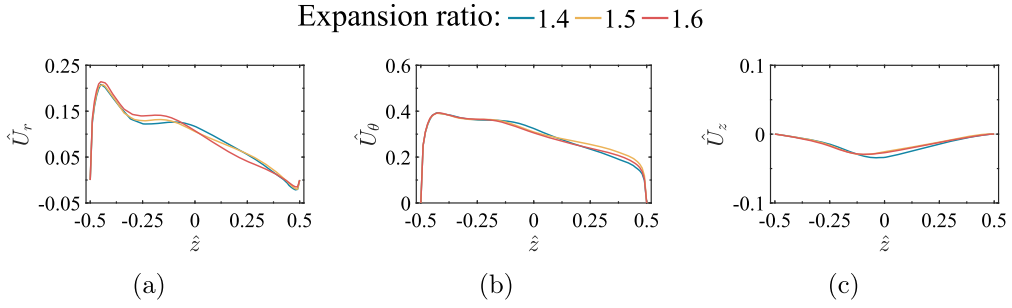

Fig. C.26. Comparison of the (a) radial, (b) tangential, and (c) axial velocity profiles in the middle of the diffuser at $r = (R_3 + R_4)/2$. The profiles are obtained for RANS simulations at the design flow rate Q_d with three different meshes that employ (blue) 13 layers with expansion ratios of 1.4, (orange) 11 layers with expansion ratios of 1.5, and (red) 10 layers with expansion ratios of 1.6.

Appendix D. Turbulence model independence analysis

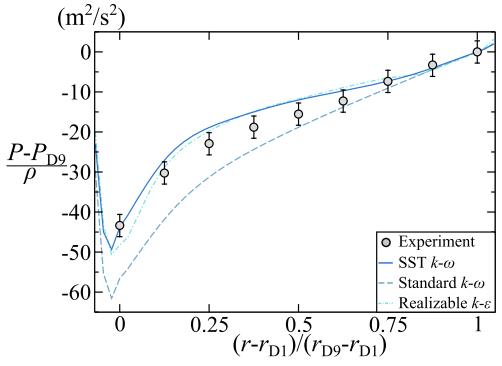

Fig. D.27. Diffuser pressure recovery of the positive-leakage case at the design condition Q_d predicted by RANS simulation of the entire pump employing different turbulence models.

Several turbulence models commonly used for the numerical simulation of turbomachinery are compared. The standard $k-\epsilon$ turbulence model is excluded due to a high y^+ requirement, hence it is not compatible with the boundary layers we aim at fitting. The turbulence model independence analysis is carried out for standard $k-\omega$, $k-\omega$ SST, and realizable $k-\epsilon$ turbulence models. The diffuser pressure recovery curves of the positive-leakage case at the design condition Q_d obtained by RANS simulations employing these three turbulence models are verified against the experimental result as shown in Fig. D.27. The results show the standard $k-\omega$ model does not correctly predict the pressure recovery in the diffuser. On the other hand, our $k-\omega$ SST and the realizable $k-\epsilon$ model provide very similar results. Therefore we choose the $k-\omega$ SST model which is considered a more suitable choice for the centrifugal pump over the realizable $k-\epsilon$ model as it takes into account the transport of the principal turbulent shear stress. The $k-\omega$ SST model has also been demonstrated as reliable, robust, and efficient for predicting global performance and capturing essential flow characteristics in centrifugal machine simulations through various examples in literature [26–30] and validated by experiments.

References

[1] W. Jansen, Rotating stall in a radial vaneless diffuser, J. Fluids Eng. 86 (4) (1964) 750–758.
[2] D. Japikse, Centrifugal Compressor Design and Performance, Wilder, Concepts ETI, VT, 1996.
[3] Y. Senoo, Y. Kinoshita, Influence of inlet flow conditions and geometries of centrifugal vaneless diffusers on critical flow angle for reverse flow, J. Fluids Eng. Trans. ASME (1977) 98–102.
[4] P. Frigne, R. Van den Braembussche, A theoretical model for rotating stall in the vaneless diffuser of a centrifugal compressor, J. Eng. Gas Turbines Power 107 (2) (1985) 507–513, https://doi.org/10.1115/1.3239760.
[5] Y. Tsujimoto, Y. Yoshida, Y. Mori, Study of vaneless diffuser rotating stall based on two-dimensional inviscid flow analysis, J. Fluids Eng. 118 (1) (1996) 123–127, https://doi.org/10.1115/1.2817489.
[6] A.N. Abdelhamid, Effects of vaneless diffuser geometry on flow instability in centrifugal compression systems, in: Turbo Expo: Power for Land Sea, and Air, vol. 101, 1981, 79610, V001T03A008.
[7] F.K. Moore, Weak rotating flow disturbances in a centrifugal compressor with a vaneless diffuser, J. Turbomach. 111 (4) (1989) 442–449.
[8] S. Ljevar, H.C.D. Lange, A.A.V. Steenhoven, Two-dimensional rotating stall analysis in a wide vaneless diffuser, Int. J. Rotating Mach. 2006 (2006) 056420.
[9] C. Gao, C. Gu, T. Wang, B. Yang, Analysis of geometries' effects on rotating stall in vaneless diffuser with wavelet neural networks, Int. J. Rotating Mach. 2007 (2007) 076476.
[10] H.-S. Dou, S. Mizuki, Analysis of the flow in vaneless diffusers with large width-to-radius ratios, J. Turbomach. 120 (1) (1998) 193–201.
[11] C. Hu, C. Yang, X. Shi, R. Zou, L. Liu, H. Chen, Investigation of rotating stall in radial vaneless diffusers with asymmetric inflow, Aerosp. Sci. Technol. 96 (2020) 105546.
[12] P. Emvin, L. Davidson, A numerical comparison of three inlet approximations of the diffuser in case E1 Annex 20, vol. 1, in: Proc. Roomvent'96, 1996, pp. 219–226.
[13] B. Deng, J. Wang, J. Tang, J. Gao, Improvement of the momentum method as the diffuser boundary condition in CFD simulation of indoor airflow: discretization viewpoint, Build. Environ. 141 (2018) 55–60.
[14] M. Fan, A. Dazin, G. Bois, F. Romanò, Effect of inlet leakage flow on the instability in a radial vaneless diffuser, Phys. Fluids 35 (1) (2023) 014105, https://doi.org/10.1063/5.0133948.
[15] M. Fan, A. Dazin, F. Romanò, G. Bois, Effect of leakage on the performance of the vaneless diffuser of a centrifugal pump model, in: Conference on Modelling Fluid Flow (CMFF'22), Budapest, Hungary, 2022, pp. 51–58.
[16] F.R. Menter, Ten years of industrial experience with the SST turbulence model, Turbul. Heat Mass Transf. 4 (2003) 625–632.
[17] A. Palumbo, F. Capuano, L. Luca, Performances of two open-source solvers in the numerical simulation of synthetic jets, in: Proceedings of the 7th European Conference on Computational Fluid Dynamics (ECCM-ECFD 2018), Glasgow, UK, 2018, pp. 11–15.
[18] F. Romanò, Stability of generalized Kolmogorov flow in a channel, Phys. Fluids 33 (2) (2021) 024106.
[19] A. Dazin, High-speed stereoscopic PIV study of rotating instabilities in a radial vaneless diffuser, Exp. Fluids 51 (2011) 83–93.
[20] S. Suzuki, U. Yoshio, H. H., Noise characteristics in partial discharge of centrifugal fans: 1st report, low-frequency noise due to the rotating stall, Bull. JSME 21 (154) (1978) 689–696.
[21] G. Caignaert, B. Desmet, D. Stevenaert, Experimental investigations on the flow in the impeller of a centrifugal fan, in: Turbo Expo: Power for Land, Sea, and Air, American Society of Mechanical Engineers, 1982, 79566, V001T01A013.
[22] A. Dazin, O. Coutier-Delgosha, P. Dupont, S. Coudert, G. Caignaert, G. Bois, Rotating instability in the vaneless diffuser of a radial flow pump, J. Therm. Sci. 17 (4) (2008), https://doi.org/10.1007/s11630-008-0368-3.
[23] G. Pavesi, A. Dazin, G. Cavazzini, G. Caignaert, G. Bois, G. Ardizzon, Experimental and numerical investigation of unforced unsteadiness in a vaneless radial diffuser, in: 9th European Conference on Turbomachinery: Fluid Dynamics and Thermodynamics, ETC 2011 - Conference Proceedings, vol. 1, 2011.
[24] Y.G. Heng, A. Dazin, M.N. Ouarzazi, Q.R. Si, Experimental study and theoretical analysis of the rotating stall in a vaneless diffuser of radial flow pump, in: IOP Conference Series: Earth and Environmental Science, vol. 49, 2016, 032006.
[25] Y. Heng, A. Dazin, M. Ouarzazi, Linear stability analysis of rotating stall in a wide vaneless diffuser, in: 12th European Conference on Turbomachinery Fluid Dynamics and Thermodynamics, ETC 2017, 2017.
[26] L. Gibson, L. Galloway, S. Spence, Assessment of turbulence model predictions for a centrifugal compressor simulation, J. Glob. Power Propuls. Soc. 1 (2017) 142–156.
[27] I. Chalghoum, H. Kanfoudi, S. Elaoud, M. Akrout, R. Zgolli, Numerical modeling of the flow inside a centrifugal pump: influence of impeller–volute interaction on velocity and pressure fields, Arab. J. Sci. Eng. 41 (11) (2016) 4463–4476.
[28] O. Borm, H.P. Kau, Unsteady aerodynamics of a centrifugal compressor stage: validation of two different CFD solvers, in: Turbo Expo: Power for Land, Sea, and Air, 2012, 44748, 2753–2764.
[29] J.H. Kim, J.H. Choi, K.Y. Kim, Design optimization of a centrifugal compressor impeller using radial basis neural network method, in: Turbo Expo: Power for Land, Sea, and Air, 2009, 48883, 443–451.
[30] M. Asuaje, F. Bakir, S. Kouidri, F. Kenyery, R. Rey, Numerical modelization of the flow in centrifugal pump: volute influence in velocity and pressure fields, Int. J. Rotating Mach. 3 (2005) 244–255.